HAL
open science

An unconventional divergence preserving Finite Volume discretization of Lagrangian ideal MHD

Walter Boscheri, Raphaël Loubère, Pierre-Henri Maire

To cite this version:

Walter Boscheri, Raphaël Loubère, Pierre-Henri Maire. An unconventional divergence preserving Finite Volume discretization of Lagrangian ideal MHD. 2023. hal-04010654v2

HAL Id: hal-04010654

https://hal.science/hal-04010654v2

Preprint submitted on 13 Aug 2023

HAL is a multi-disciplinary open access archive for the deposit and dissemination of scientific research documents, whether they are published or not. The documents may come from teaching and research institutions in France or abroad, or from public or private research centers.

L'archive ouverte pluridisciplinaire **HAL**, est destinée au dépôt et à la diffusion de documents scientifiques de niveau recherche, publiés ou non, émanant des établissements d'enseignement et de recherche français ou étrangers, des laboratoires publics ou privés.

An unconventional divergence preserving Finite Volume discretization of Lagrangian ideal MHD

Walter Boscheri[1†], Raphaël Loubère[2†] and Pierre-Henri Maire[3*†]

[1]Dipartimento di Matematica e Informatica, University of Ferrara, Ferrara, Italy.
[2]Institut de Mathématiques de Bordeaux (IMB), University of Bordeaux, Talence, France.
[3*]CEA-CESTA, Le Barp, France.

*Corresponding author(s). E-mail(s): pierre-henri.maire@cea.fr;
Contributing authors: walter.boscheri@unife.it;
raphael.loubere@u-bordeaux.fr;
†These authors contributed equally to this work.

Abstract

We construct an unconventional divergence preserving discretization of updated Lagrangian ideal MHD over simplicial grids. The cell-centered FV method employed to discretize the conservation laws of volume, momentum and total energy is rigorously the same than the one developed to simulate hyperelasticity equations. By construction this moving mesh method ensures the compatibility between the mesh displacement and the approximation of the volume flux by means of the nodal velocity and the attached unit corner normal vector which is nothing but the partial derivative of the cell volume with respect to the node coordinate under consideration. This is precisely the definition of the compatibility with the Geometrical Conservation Law which is the cornerstone of any proper multi-dimensional moving mesh FV discretization. The momentum and the total energy fluxes are approximated utilizing the partition of cell faces into sub-faces and the concept of sub-face force which is the traction force attached to each sub-face impinging at a node. We observe that the time evolution of the magnetic field might be

simply expressed in terms of the deformation gradient which characterizes the Lagrange-to-Euler mapping. In this framework the divergence of the magnetic field is conserved with respect to time thanks to Piola formula. Therefore, we solve the fully compatible updated Lagrangian discretization of the deformation gradient tensor for updating in a simple manner the cell-centered value of the magnetic field. Finally, the sub-face traction force is expressed in terms of the nodal velocity to ensure a semi-discrete entropy inequality within each cell. The conservation of momentum and total energy is recovered prescribing the balance of all the sub-face forces attached to the sub-faces impinging at a given node. This balance corresponds to a vectorial system satisfied by the nodal velocity. It always admits a unique solution which provides the nodal velocity. The robustness and the accuracy of this unconventional FV scheme has been demonstrated employing various representative test cases. Finally, it is worth emphasizing that once you have an updated Lagrangian code for solving hyperelasticity you also get an almost free updated Lagrangian code for solving ideal MHD ensuring exactly the compatibility with the involution constraint for the magnetic field at the discrete level.

Keywords: Cell-centered Lagrangian finite volume schemes, hyper-elasticity, ideal MHD equations, moving unstructured meshes, *a posteriori* MOOD limiting.

1 Introduction

The physical modeling of magnetized plasma flows is of great importance for High Energy Density Physics (Inertial Confinement Fusion, Magnetic Confinement Fusion, Astrophysics). The underlying physical model is that of magnetohydrodynamics (MHD) which describes the temporal evolution of an electrically conducting fluid undergoing the action of magnetic fluid. For a fluid characterized by a high electrical conductivity one can employ the ideal MHD model which amounts to couple the compressible Euler equations with the Maxwell equations through the Lorentz force. The interested reader might refer to [1, 2] for a detailed presentation of this subtle and interesting topic. The ideal MHD consists of a system of conservation laws ruling the conservation of mass, momentum, total energy and the time evolution of the magnetic field plus the supplementary equation expressing the divergence free nature of the magnetic field due to the absence of magnetic monopoles. This additional equation is called an involution, that is, if satisfied at initial time, it is satisfied for all future times. The eigenvalues analysis of the Jacobian matrix of the flux of this system of conservation laws shows that it is hyperbolic. The solutions are quite complex and consist of various types of waves depending on the strength of the magnetic field [1, 3, 4]. Let us notice that the conservative form of the MHD equations cannot be symmetrized by the classical physical entropy and is neither Galilean invariant. Symmetrizability and Galilean invariance are recovered adding source terms proportional to the divergence of

the magnetic field leading to a non conservative form of the MHD equations known as the Godunov-Powell form of MHD after the names of its founders [5, 6]. The reader interested in these subtle concepts might find more details in [7].

The construction of numerical methods to properly simulate ideal MHD still remains a challenging and active subject. The main underlying difficulty in this task consists in controlling the growth of numerically caused magnetic field divergence errors. Indeed, ensuring the divergence free constraint of the magnetic field at the discrete level is far from being a trivial job! Several methods have been proposed in the literature to cure this problem, without being exhaustive we can quote:

- The projection method which consists in projecting the magnetic field onto a space of divergence free vectors [8];
- The Godunov-Powell approach [5, 9] wherein the ideal MHD equations are supplemented with non-conservative source terms proportional to the divergence of the magnetic field. This formulation allows to advect the numerical divergence errors away;
- The constraint transport method [10, 11] which ensures the divergence free constraint at the discrete level employing a staggered grid discretization of the magnetic field equation;
- The hyperbolic divergence cleaning [12] which relies on the coupling of the divergence constraint with the conservation laws by introducing a generalized Lagrange multiplier.

These procedures work quite well and are extensively used in MHD simulation codes. However, this is not the end of the story and there is still nowadays a lot of efforts of the community devoted to the design of robust and accurate numerical methods for solving efficiently compressible multidimensional MHD flows. Among these methods, the Finite Volume (FV) approach has been quite successfully employed and thus thoroughly investigated. It relies on the use of an approximate Riemann solver to design a consistent numerical flux at the cell interfaces following the methodology introduced by Harten, Lax and van Leer (HLL) [13]. Since the seminal work presented in [14], the construction of reliable approximate Riemann solvers for ideal MHD has motivated several major developments. We shall quote only few of them. The interested reader might refer to the bibliography proposed in [2]. For instance, [15] has introduced the notion of simple approximate Riemann solver which allows to derive systematically approximate Riemann solvers for the Eulerian one-dimensional ideal MHD from their Lagrangian counterparts employing a discrete Lagrange-to-Euler transformation. In this framework, the wave speeds of the Lagrangian solver are monitored to ensure its positivity preserving and entropy stability properties. By construction, these good properties are naturally transferred to the Eulerian solver thanks to the discrete Lagrange-to-Euler mapping. The HLLC extension to MHD equations has been achieved in [16]. We also quote

the works [17–19] devoted to the construction of multi-dimensional HLL Riemann solvers for MHD flows. Multi-wave HLL approximate Riemann solvers for ideal MHD based on relaxation are investigated in [20] and supplemented with conditions on the relaxation parameters to ensure positivity of density and internal energy and also an entropy inequality. The numerical implementation of these solvers are described in [21]. In [22] the authors proposed a family of approximate Riemann solvers (three- and five-wave) for the Powell form of the MHD equations. These solvers are of the HLL type and take into account a varying normal magnetic field. More recently, [23] proposed to extend the ideal MHD equations with an inbuilt divergence cleaning mechanism consistently with the second law of thermodynamics. In [24] the authors described Discontinuous Galerkin and FV methods for ideal MHD which provably preserve the positivity of density and pressure on general grids employing a proper discretization of the symmetrizable MHD system and consistently controlling the divergence of the magnetic field.

We observe that most of the numerical developments are dedicated to the ideal MHD equations written under the Eulerian form, whereas few works have been undertaken to cope with the updated Lagrangian MHD which is a moving mesh method. Among them, let us mention the recent work [25] wherein a 3D cell-centered Lagrangian FV scheme is constructed for solving ideal MHD equations over unstructured grids. The underlying numerical method stems from the compatible cell-centered discretization introduced for Lagrangian hydrodynamics [26, 27]. The divergence free constraint of the magnetic field is enforced by means of a costly projection method which requires to solve an elliptic Poisson equation after each time step. A partial Runge-Kutta Discontinuous Galerkin method for solving the 2D ideal MHD equation written under updated Lagrangian form is described in [28]. This numerical method is characterized by an exactly divergence-free magnetic field at the discrete level. This results from the use of the integral form of the magnetic field equation which states that the magnetic flux through a Lagrangian surface remains constant by virtue of the frozen-in flux theorem. In addition, it is worth quoting the theoretical work [29] wherein a new Lagrangian formulation of ideal magnetohydrodynamics is proposed. This original formulation consists in rewriting the ideal MHD employing a total Lagrangian representation of hyperelasticity with an *ad hoc* thermodynamic potential such that the Piola-Kirchoff stress tensor coincides with the magnetic stress tensor. This fruitful analogy allows to show the hyperbolicity of the Lagrangian ideal MHD without divergence free constraint.

Inspired by these latter works, we propose in the present paper an unconventional divergence preserving discretization of updated Lagrangian ideal MHD over simplicial grids. The cell-centered FV method employed to discretize the conservation laws of volume, momentum and total energy is rigorously the same than the one developed in our previous paper [30] to simulate the hyperelasticity equations. By construction this moving mesh method

ensures the compatibility between the mesh displacement and the approximation of the volume flux by means of the nodal velocity and the unit corner normal vector attached which is nothing but the partial derivative of the cell volume with respect to the node coordinate under consideration. This is precisely the definition of the compatibility with the Geometrical Conservation Law which is the cornerstone of any proper multi-dimensional moving mesh FV discretization [31]. The momentum and the total energy fluxes are approximated utilizing the partition of cell faces into sub-faces and the concept of sub-face force which is the traction force attached to each sub-face impinging at a node. We observe that the time evolution of the magnetic field might be simply expressed in terms of the deformation gradient which characterizes the Lagrange-to-Euler mapping. In this framework the divergence of the magnetic field is conserved with respect to time thanks to Piola formula. Therefore, we solve the fully compatible updated Lagrangian discretization of the deformation gradient tensor initially proposed in [30] for updating in a simple manner the cell-centered value of the magnetic field. Finally, the sub-face traction force is expressed in terms of the nodal velocity to ensure a semi-discrete entropy inequality within each cell. The conservation of momentum and total energy is recovered prescribing the balance of all the sub-face forces attached to the sub-faces impinging at a given node. This balance corresponds to a vectorial system satisfied by the nodal velocity. It always admits a unique solution which provides the nodal velocity. The high-order extension of this numerical method is achieved thanks to an ADER-MOOD methodology [30]. The robustness and the accuracy of this unconventional FV scheme have been demonstrated employing various representative test cases. Finally, it is worth emphasizing that once you have an updated Lagrangian code for solving hyperelasticity you also get an almost free updated Lagrangian code for solving ideal MHD ensuring the compatibility of the magnetic field with the involution constraint at the discrete level.

The rest of this paper is organized as follows. Section 2 is devoted to the presentation of the governing equations of ideal MHD. Section 3 deals with updated Lagrangian form of ideal MHD and the links with updated Lagrangian hyperelasticity relying on the expression of the magnetic field in terms of the deformation gradient tensor characterizing the Lagrange-to-Euler mapping. Then, in section 4 the Finite Volume method initially developed for updated Lagrangian hyperelasticity is recalled and adapted to the ideal MHD context. The high-order ADER-MOOD methodology for ideal MHD is described in section 5. Finally, the robustness and the accuracy of this unconventional discretization of Lagrangian ideal MHD are assessed against a large set of classical MHD numerical test cases run in 1D, 2D and 3D on unstructured grids. The results are presented and commented in section 6 with a particular emphasis on the preservation of the magnetic field divergence at the discrete level. At last, conclusions and perspectives are drawn.

2 Governing equations

2.1 Ideal MHD equations

The ideal magnetohydrodynamics (MHD) equations describe the temporal evolution of a quasi-neutral plasma flow subject to a magnetic field $\boldsymbol{B}$ and neglecting the viscous and resistive effects. The interesting reader might refer to the lecture notes [1] for a detailed derivation of MHD. These equations are written under the form of the following set of conservation laws

$$\frac{\partial \rho}{\partial t} + \nabla \cdot (\rho \boldsymbol{v}) = 0, \tag{1a}$$

$$\frac{\partial \rho \boldsymbol{v}}{\partial t} + \nabla \cdot [\rho(\boldsymbol{v} \otimes \boldsymbol{v}) + P_t \mathbb{I}_{\mathrm{d}}] - \nabla \cdot \left[\frac{1}{\mu_0}(\boldsymbol{B} \otimes \boldsymbol{B})\right] = \boldsymbol{0}, \tag{1b}$$

$$\frac{\partial \rho E}{\partial t} + \nabla \cdot [(\rho E + P_t)\boldsymbol{v}] - \nabla \cdot \left[\frac{1}{\mu_0}(\boldsymbol{B} \cdot \boldsymbol{v})\boldsymbol{B}\right] = 0. \tag{1c}$$

Let us note that these equations respectively express the conservation of mass, momentum and total energy. All the physical quantities are expressed in terms of the time $t \geq 0$ and the Eulerian coordinate $\boldsymbol{x} \in \mathbb{R}^{\mathrm{d}}$ where d is the space dimension. Here, $\rho > 0$ is the mass density and $\boldsymbol{v}$ is the velocity field. The total pressure P_t is the sum of the thermodynamic pressure and the magnetic pressure

$$P_t = p + \frac{\boldsymbol{B}^2}{2\mu_0}. \tag{2}$$

The unit tensor of $\mathbb{R}^{\mathrm{d}}$ is denoted by $\mathbb{I}_{\mathrm{d}}$ and μ_0 is the vacuum magnetic permeability which is constant. The specific total energy of the magnetic fluid writes as the sum of the specific total energy and the magnetic energy

$$E = e + \frac{\boldsymbol{B}^2}{2\mu_0 \rho}, \tag{3}$$

and the specific total energy, e, is nothing but the sum of the specific internal energy, ε, and the kinetic one

$$e = \varepsilon + \frac{1}{2}\boldsymbol{v}^2. \tag{4}$$

The temporal evolution of the magnetic field is deduced from the Maxwell equations [1] and reads

$$\frac{\partial \boldsymbol{B}}{\partial t} - \nabla \times (\boldsymbol{v} \times \boldsymbol{B}) = 0. \tag{5}$$

The foregoing set of equations is usually supplemented by writing that the magnetic field satisfies the divergence constraint

$$\nabla \cdot \boldsymbol{B} = 0. \tag{6}$$

This describes the absence of magnetic monopole. Such a magnetic field is said to be solenoidal or divergence free. Finally, (1), (5) and (6) are the ideal MHD equations. We observe that taking the divergence of (5) yields

$$\frac{\partial(\nabla \cdot \boldsymbol{B})}{\partial t} = 0.$$

If the magnetic field is divergence free initially then it remains so. Hence, constraint (6) is named involutive.

The thermodynamic closure of (1) is expressed by means of the complete equation of state (EOS) which definition relies on the fundamental assumption that $(\tau, \eta) \longmapsto \varepsilon(\tau, \eta)$ is strictly convex, where $\tau = 1/\rho$ is the specific volume and η the specific entropy. This amounts to assume that $(\tau, \varepsilon) \longmapsto \eta(\tau, \varepsilon)$ is strictly concave [32] and we are considering the physical entropy. The thermodynamic pressure, p, and temperature, θ, are defined in terms of (τ, η) as

$$p = -\frac{\partial \varepsilon}{\partial \tau}|_\eta, \text{ and } \theta = \frac{\partial \varepsilon}{\partial \eta}|_\tau, \tag{7}$$

where we assume that $\theta > 0$. The convexity assumption allows us to define the isentropic sound speed

$$\frac{\alpha^2}{\tau^2} = -\frac{\partial p}{\partial \tau}|_\eta = \frac{\partial \varepsilon^2}{\partial \tau^2}|_\eta > 0. \tag{8}$$

2.2 The continuum mechanics-like form of the MHD equations

Introducing the pseudo stress tensor

$$\mathbb{T} = -P_t \mathbb{I}_\mathrm{d} + \frac{\boldsymbol{B} \otimes \boldsymbol{B}}{\mu_0} \tag{9}$$

allows us to rewrite the MHD system (1) under the compact form

$$\frac{\partial \rho}{\partial t} + \nabla \cdot (\rho \boldsymbol{v}) = 0, \tag{10a}$$

$$\frac{\partial \rho \boldsymbol{v}}{\partial t} + \nabla \cdot \rho(\boldsymbol{v} \otimes \boldsymbol{v}) - \nabla \cdot \mathbb{T} = \boldsymbol{0}, \tag{10b}$$

$$\frac{\partial \rho E}{\partial t} + \nabla \cdot (\rho E \boldsymbol{v}) - \nabla \cdot (\mathbb{T} \boldsymbol{v}) = 0. \tag{10c}$$

Written under the foregoing form, the MHD equations are completely similar to the classical conservation laws of continuum mechanics. The difference lies uniquely in the expression of the pseudo stress tensor $\mathbb{T}$. In what follows, we shall explore further this analogy writing the foregoing equations under updated Lagrangian representation and showing their connection with the conservation laws of updated Lagrangian hyperelasticity, refer for instance to [30].

2.3 Gibbs relation associated to MHD

We aim at writing the fundamental relation expressing the differential of the specific entropy in terms of the differential of the variables $(\tau, \boldsymbol{v}, \tau\boldsymbol{B}, E)$. This shall be useful for deriving the entropy balance in section 3.4. First, differentiating $\varepsilon(\tau, \eta)$ with respect to τ and η yields

$$\mathrm{d}\varepsilon = \frac{\partial \varepsilon}{\partial \tau}|_{\eta}\mathrm{d}\tau + \frac{\partial \varepsilon}{\partial \eta}|_{\tau}\mathrm{d}\eta,$$

which, by definition of the EOS, rewrites as

$$\theta \mathrm{d}\eta = p\mathrm{d}\tau + \mathrm{d}\varepsilon. \tag{11}$$

This is the well known Gibbs relation. Now, combining (4) and (3) we express the specific internal energy as follows

$$\varepsilon = E - \frac{\boldsymbol{B}^2}{2\mu_0\rho} - \frac{1}{2}\boldsymbol{v}^2.$$

Substituting the foregoing expression into the Gibbs relation (11) turns it into

$$\theta \mathrm{d}\eta = p\mathrm{d}\tau - \frac{1}{2\mu_0}\mathrm{d}\left(\frac{\boldsymbol{B}^2}{\rho}\right) - \boldsymbol{v}\cdot\mathrm{d}\boldsymbol{v} + \mathrm{d}E.$$

Recalling that $\tau = \frac{1}{\rho}$ we arrive at the MHD Gibbs relation

$$\theta \mathrm{d}\eta = \left(p + \frac{\boldsymbol{B}^2}{2\mu_0}\right)\mathrm{d}\tau - \boldsymbol{v}\cdot\mathrm{d}\boldsymbol{v} - \frac{\boldsymbol{B}}{\mu_0}\mathrm{d}\left(\frac{\boldsymbol{B}}{\rho}\right) + \mathrm{d}E. \tag{12}$$

3 Updated Lagrangian form of MHD

The aim of this section is to write the MHD system composed of (10) and (5) under the updated Lagrangian form. Before going any further, we start by recalling geometrical notions characterizing the Lagrange-to-Euler mapping. The interested reader might refer to [33] for a more detailed presentation of this topic.

3.1 Total and updated Lagrangian representations

Let us consider a fluid particle in the initial configuration at time $t = 0$ characterized by its coordinate $\boldsymbol{X}$ named material or Lagrangian coordinate. At time $t > 0$ this fluid particle is located at position $\boldsymbol{x}$, named the spatial or Eulerian coordinate. The Lagrange-to-Euler mapping transforms $\boldsymbol{X}$ into $\boldsymbol{x}$

$$\boldsymbol{\Phi} : \boldsymbol{X} \longmapsto \boldsymbol{x} = \boldsymbol{\Phi}(\boldsymbol{X}, t).$$

This transformation is such that $\mathrm{d}\boldsymbol{\Phi}$ is an exact differential

$$\mathrm{d}\boldsymbol{\Phi} = \mathbb{F}\mathrm{d}\boldsymbol{X} + \boldsymbol{v}\mathrm{d}t, \quad \text{where} \quad \mathbb{F} = \frac{\partial \boldsymbol{\Phi}}{\partial \boldsymbol{X}}|_t \quad \text{and} \quad \boldsymbol{v} = \frac{\partial \boldsymbol{\Phi}}{\partial t}|_{\boldsymbol{X}}. \tag{13}$$

Here, $\mathbb{F}$ is the deformation gradient tensor and $\boldsymbol{v}$ is the kinematic velocity which satisfy the compatibility condition

$$\frac{\partial \mathbb{F}}{\partial t} - \nabla_X \boldsymbol{v} = 0. \tag{14}$$

This is nothing but the Geometrical Conservation Law (GCL). Let us point out that ∇_X is the nabla operator acting on the Lagrangian coordinate. At time $t = 0$ we have $\mathbb{F}(\boldsymbol{X}, 0) = \mathbb{I}_\mathrm{d}$ and introducing $J = \det \mathbb{F}$ we get $J(\boldsymbol{X}, 0) = 1$. By a continuity argument we assume that $J(\boldsymbol{X}, t) > 0$ for $t > 0$. This ensures the invertibility of the Lagrange-to-Euler transformation which is thus a one-to-one mapping.

Next, if $f \equiv f(\boldsymbol{X}, t)$ is a physical quantity attached to the material, its value at $\boldsymbol{x} = \boldsymbol{\Phi}(\boldsymbol{X}, t)$ is also denoted employing the same notation. This amounts to write

$$f(\boldsymbol{X}, t) = f(\boldsymbol{x}, t), \quad \text{where} \quad \boldsymbol{x} = \boldsymbol{\Phi}(\boldsymbol{X}, t).$$

Taking the time derivative of the foregoing equation holding $\boldsymbol{X}$ fixed leads to

$$\begin{aligned} \frac{\partial f}{\partial t}(\boldsymbol{x}, t)|_{\boldsymbol{X}} =& \frac{\partial f}{\partial t}(\boldsymbol{x}, t)|_{\boldsymbol{x}} + \frac{\partial \boldsymbol{\Phi}}{\partial t} \cdot \nabla_x f \\ =& \frac{\partial f}{\partial t}(\boldsymbol{x}, t)|_{\boldsymbol{x}} + \boldsymbol{v} \cdot \nabla_x f. \end{aligned}$$

The first term at the left (resp. right) hand side is the Lagrangian (resp. Eulerian) time derivative. This leads to introduce the material derivative which coincides with the Lagrangian time derivative for $f(\boldsymbol{x}, t)$ where $\boldsymbol{x} = \boldsymbol{\Phi}(\boldsymbol{X}, t)$

$$\frac{\mathrm{d}f}{\mathrm{d}t} = \frac{\partial f}{\partial t}(\boldsymbol{x}, t)|_{\boldsymbol{x}} + \boldsymbol{v} \cdot \nabla_x \cdot f. \tag{15}$$

The extension of (15) to vector reads

$$\frac{\mathrm{d}\boldsymbol{w}}{\mathrm{d}t} = \frac{\partial \boldsymbol{w}}{\partial t}(\boldsymbol{x}, t)|_{\boldsymbol{x}} + (\nabla_x \boldsymbol{w})\boldsymbol{v}. \tag{16}$$

Realizing that $\dfrac{\mathrm{d}}{\mathrm{d}t} = \dfrac{\partial}{\partial t}|_{\boldsymbol{X}}$ we rewrite the GCL (14) under its updated Lagrangian form

$$\frac{\mathrm{d}\mathbb{F}}{\mathrm{d}t} - (\nabla_x \boldsymbol{v})\mathbb{F} = 0, \tag{17}$$

since $\nabla_X \boldsymbol{v} \equiv (\nabla_x \boldsymbol{v})\mathbb{F}$ thanks to the chain rule of composed derivative.

We pursue recalling the Piola formula which allows to express the Eulerian divergence operator, *i.e.* $\nabla_x \cdot ()$, in terms of its Lagrangian counterpart, *i.e.*

$\nabla_X \cdot ()$, in terms of the deformation gradient tensor. This formula shall be of great interest to give a geometrical interpretation of the divergence constraint related to the magnetic field. To this end, let us consider the volume Ω in the initial configuration and its image $\omega(t)$ by the transformation $\boldsymbol{\Phi}$ at time $t > 0$, that is $\omega = \boldsymbol{\Phi}(\Omega, t)$, refer to figure 1. The volume element $\mathrm{d}V$ and the surface element $\boldsymbol{N}\mathrm{d}S$ transform as follows [33]

$$\mathrm{d}v = J\,\mathrm{d}V, \text{ and } \boldsymbol{n}\mathrm{d}s = J\mathbb{F}^{-t}\boldsymbol{N}\,\mathrm{d}S, \text{ Nanson formula.} \tag{18}$$

Here, $\boldsymbol{N}$ and $\boldsymbol{n}$ are the outward pointing unit normals to Ω and ω respectively. Employing this transformation formulas we investigate the relation between the Eulerian and the Lagrangian divergence operators. Applying the divergence theorem to any vector $\boldsymbol{w}$ yields

$$\begin{aligned}
\int_\omega \nabla_x \cdot \boldsymbol{w}\,\mathrm{d}v &= \int_{\partial\omega} \boldsymbol{w}\cdot\boldsymbol{n}\,\mathrm{d}s \\
&= \int_{\partial\Omega} \boldsymbol{w}\cdot\left(J\mathbb{F}^{-t}\right)\boldsymbol{N}\,\mathrm{d}S, \text{ thanks to Nanson formula} \\
&= \int_{\partial\Omega} J\mathbb{F}^{-1}\boldsymbol{w}\cdot\boldsymbol{N}\,\mathrm{d}S \\
&= \int_{\Omega} \nabla_X \cdot \left(J\mathbb{F}^{-1}\boldsymbol{w}\right)\,\mathrm{d}V.
\end{aligned}$$

Moreover, recalling that $\int_\omega \nabla_x \cdot \boldsymbol{w}\,\mathrm{d}v = \int_\Omega \nabla_x \cdot \boldsymbol{w}\,J\,\mathrm{d}V$, we arrive at the well known Piola's formula

$$\nabla_x \cdot \boldsymbol{w} = J^{-1}\nabla_X \cdot \left(J\mathbb{F}^{-1}\boldsymbol{w}\right). \tag{19}$$

Remark 1. *For $\boldsymbol{w}$ constant Piola formula (19) boils down to the so called Piola compatibility condition*

$$\nabla_X \cdot \left(J\mathbb{F}^{-t}\right) = \boldsymbol{0}, \tag{20}$$

since $\nabla_X \cdot \left(J\mathbb{F}^{-1}\boldsymbol{w}\right) = \boldsymbol{w}\cdot\nabla_X\cdot(J\mathbb{F}^{-t}) + J\mathbb{F}^{-t} : \nabla_X\boldsymbol{w}$, where for tensors we denote $\mathbb{A} : \mathbb{B} = tr(\mathbb{A}^t\mathbb{B})$. Applying the divergence theorem to (20) we realize that the Piola compatibility equation simply means that the integral of the Eulerian normal $\boldsymbol{n}$ along the closed contour $\partial\omega$ vanishes.

Remark 2. *If one solves the GCL (14) to compute $\mathbb{F}$ one must ensure that $\mathbb{F}$ derives from a mapping by checking the compatibility condition $\nabla_X \times \mathbb{F} = 0$. This is an involutive constraint attached to (14), i.e, if it is satisfied at $t = 0$, then it is for any $t > 0$ since by applying the $\nabla_X\times$ operator to (14) one gets*

$$\frac{\partial}{\partial t}\left(\nabla_X \times \mathbb{F}\right) = 0.$$

We underline here the equivalence between the condition $\nabla_X \times \mathbb{F} = 0$ *and the Piola condition* $\nabla_X \cdot (J\mathbb{F}^{-t}) = \mathbf{0}$*, refer for instance to [34] where these conditions are employed to derive a Discontinuous Galerkin discretization of gas dynamics written under total Lagrangian form.*

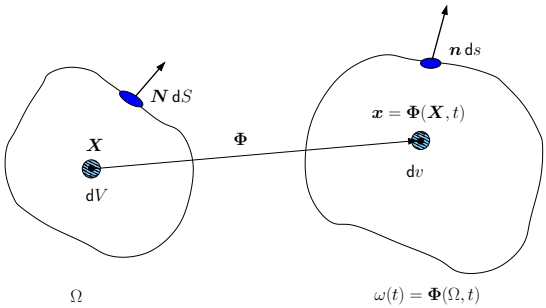

Fig. 1 Sketch of the Lagrange-to-Euler transformation which maps the material Lagrangian point $\boldsymbol{X}$ onto its Eulerian counterpart $\boldsymbol{x}$, *i.e.* $\boldsymbol{x} = \boldsymbol{\Phi}(\boldsymbol{X}, t)$.

3.2 Updated Lagrangian form of the system of conservation laws

Introducing the material derivatives (15) and (16) into the Eulerian form of the MHD system of conservation laws (10) we arrive at its updated Lagrangian representation

$$\rho \frac{\mathrm{d}\tau}{\mathrm{d}t} - \nabla_x \cdot \boldsymbol{v} = 0, \tag{21a}$$

$$\rho \frac{\mathrm{d}\boldsymbol{v}}{\mathrm{d}t} - \nabla_x \cdot \mathbb{T} = \mathbf{0}, \tag{21b}$$

$$\rho \frac{\mathrm{d}E}{\mathrm{d}t} - \nabla_x \cdot (\mathbb{T}\boldsymbol{v}) = 0, \tag{21c}$$

where the stress tensor, $\mathbb{T}$, is still defined by (9). This is the MHD system of conservation laws written under updated Lagrangian representation. It is supplemented by the trajectory equation already introduced in (13), which is rewritten under the form

$$\frac{\mathrm{d}\boldsymbol{x}}{\mathrm{d}t} = \boldsymbol{v}(\boldsymbol{x}(t), t), \qquad \boldsymbol{x}(0) = \boldsymbol{X}. \tag{22}$$

We observe that (21a) is the volume conservation equation which stems from the combination of the Lagrangian mass conservation equation, $\dfrac{\mathrm{d}(\rho J)}{\mathrm{d}t} = 0$, and the GCL (17) since $J = \det \mathbb{F}$.

3.3 Kinematics of the magnetic field

In this paragraph we derive the updated Lagrangian form of the magnetic field evolution equation (5) which reads

$$\frac{\partial \boldsymbol{B}}{\partial t} - \nabla_x \times (\boldsymbol{v} \times \boldsymbol{B}) = \boldsymbol{0}.$$

In what follows, we assume a sufficient smoothness of the velocity and the magnetic fields to allow all the subsequent algebraic developments. Bearing this in mind, we shall provide a kinematic interpretation of the magnetic field equation that will be particularly useful to solve it explicitly employing the GCL (17). First, we recall the vectorial identities

$$\begin{aligned}\nabla_x \times (\boldsymbol{v} \times \boldsymbol{B}) =& \nabla_x \cdot (\boldsymbol{v} \otimes \boldsymbol{B} - \boldsymbol{B} \otimes \boldsymbol{v}),\\ \nabla_x \cdot (\boldsymbol{B} \otimes \boldsymbol{v}) =& \boldsymbol{B} \nabla_x \cdot \boldsymbol{v} + (\nabla_x \boldsymbol{B})\boldsymbol{v}.\end{aligned}$$

Then, combining these identities and using the divergence free constraint (6) we can rewrite the magnetic field evolution equation (5) as

$$\frac{\partial \boldsymbol{B}}{\partial t} + (\nabla_x \boldsymbol{B})\boldsymbol{v} + \boldsymbol{B}\nabla_x \cdot \boldsymbol{v} - (\nabla_x \boldsymbol{v})\boldsymbol{B} = \boldsymbol{0}.$$

Next, employing the definition of the material derivative (16) and the conservation equation (21a) we get

$$\frac{\mathrm{d}}{\mathrm{d}t}\left(\frac{\boldsymbol{B}}{\rho}\right) - (\nabla_x \boldsymbol{v})\left(\frac{\boldsymbol{B}}{\rho}\right) = \boldsymbol{0}. \tag{23}$$

This is exactly the same equation satisfied by a material line element advected and distorted by the fluid motion. This is also the equation satisfied by the vorticity $\nabla_x \times \boldsymbol{v}$ in homoentropic or barotropic fluids in the absence of a magnetic field, refer to [1, 33].

We pursue the transformation of the foregoing equation noticing that by the virtue of the GCL equation written under updated Lagrangian form (17), the velocity gradient is expressed in terms of the deformation gradient

$$\nabla_x \boldsymbol{v} = -\mathbb{F}\frac{\mathrm{d}\mathbb{F}^{-1}}{\mathrm{d}t},$$

since $\mathbb{F}$ is invertible and $\frac{\mathrm{d}}{\mathrm{d}t}(\mathbb{F}^{-1}\mathbb{F}) = 0$. Now, substituting this expression of the velocity gradient into (23) leads to

$$\mathbb{F}^{-1}\frac{\mathrm{d}}{\mathrm{d}t}\left(\frac{\boldsymbol{B}}{\rho}\right) + \frac{\mathrm{d}\mathbb{F}^{-1}}{\mathrm{d}t}\left(\frac{\boldsymbol{B}}{\rho}\right) = \boldsymbol{0},$$

which is equivalent to

$$\frac{\mathrm{d}}{\mathrm{d}t}\left(\mathbb{F}^{-1}\frac{\boldsymbol{B}}{\rho}\right) = \mathbf{0},$$

and after time integration yields

$$\mathbb{F}^{-1}\frac{\boldsymbol{B}}{\rho} = \frac{\boldsymbol{B}^0}{\rho^0}, \text{ since } \mathbf{F}(\boldsymbol{X},0) = \mathbf{I}_\mathrm{d}.$$

Here, $\boldsymbol{B}^0 = \boldsymbol{B}^0(\boldsymbol{X})$ and $\rho^0 = \rho^0(\boldsymbol{X})$ are respectively the initial magnetic field and the initial density. The Lagrangian mass conservation $\rho J = \rho^0$ allows us to write the analytical expression of the current magnetic field in terms of the deformation gradient

$$\boldsymbol{B}(\boldsymbol{x},t) = J^{-1}(\boldsymbol{X},t)\mathbb{F}(\boldsymbol{X},t)\boldsymbol{B}^0(\boldsymbol{X}), \tag{24}$$

where $\boldsymbol{x} = \boldsymbol{\phi}(\boldsymbol{X},t)$. This exhibits the frozen character of the magnetic field which is simply convected as a material line element through the Lagrange-to-Euler transformation.

Knowing the analytical expression of the magnetic field, let us compute its divergence. This is achieved through the use of the Piola transformation formula (19), which allows to express the divergence of the current magnetic field at time $t > 0$ in terms of its initial divergence

$$\nabla_x \cdot \boldsymbol{B} = J^{-1}\,\nabla_X \cdot \left(J\mathbb{F}^{-1}\boldsymbol{B}\right) = J^{-1}\,\nabla_X \cdot \left(J\mathbb{F}^{-1}J^{-1}\mathbb{F}\boldsymbol{B}^0\right).$$

Finally, the divergence of the analytical magnetic field given by (24) is preserved through time

$$\nabla_x \cdot \boldsymbol{B} = J^{-1}\,\nabla_X \cdot \boldsymbol{B}^0. \tag{25}$$

Thus, if $\boldsymbol{B}$ is initially divergence free, it remains so for all time $t > 0$. This means that the analytical magnetic field given by (24) satisfies the involutive constraint by construction.

Inspired by this result obtained at the continuous level, we shall construct a spatial discretization of the MHD equations wherein the cell-centered magnetic field shall be computed employing the discrete counterpart of (24). The underlying cell-centered deformation gradient shall be deduced from a compatible spatial discretization of the GCL (17) identical to the one introduced in our previous work [30] devoted to the Finite Volume discretization of the Lagrangian hyperelasticity equations.

Remark 3. *Integrating* (25) *over the Eulerian control volume* $\omega(t)$ *leads to*

$$\int_{\omega(t)} \nabla_x \boldsymbol{B}\,\mathrm{d}v = \int_\Omega \nabla_X \cdot \boldsymbol{B}^0\,\mathrm{d}V,$$

where Ω is the Lagrangian counterpart of $\omega(t)$, i.e., $\omega(t) = \boldsymbol{\phi}(\Omega, t)$. Then, applying the divergence theorem for both left and right-hand sides, we get

$$\int_{\partial\omega(t)} \boldsymbol{B} \cdot \boldsymbol{n} \, \mathrm{d}s = \int_{\partial\Omega} \boldsymbol{B}^0 \cdot \boldsymbol{N} \, \mathrm{d}S, \tag{26}$$

which expresses the conservation of the magnetic field flux with respect to time.

3.4 Updated Lagrangian form of the entropy balance

The differential form of the Gibbs relationship (12) provides us the entropy balance under updated Lagrangian form

$$\rho\theta \frac{\mathrm{d}\eta}{\mathrm{d}t} = \left(p + \frac{\boldsymbol{B}^2}{2\mu_0}\right) \rho \frac{\mathrm{d}\tau}{\mathrm{d}t} - \boldsymbol{v} \cdot \rho \frac{\mathrm{d}\boldsymbol{v}}{\mathrm{d}t} - \frac{\boldsymbol{B}}{\mu_0} \cdot \rho \frac{\mathrm{d}}{\mathrm{d}t}\left(\frac{\boldsymbol{B}}{\rho}\right) + \rho \frac{\mathrm{d}E}{\mathrm{d}t}.$$

Now, substituting (21a), (21b), (23) and (21c) into the foregoing equation yields

$$\begin{aligned} \rho\theta \frac{\mathrm{d}\eta}{\mathrm{d}t} &= \left(p + \frac{\boldsymbol{B}^2}{2\mu_0}\right) \nabla_x \cdot \boldsymbol{v} - \boldsymbol{v} \cdot \nabla_x \cdot \mathbb{T} - \frac{\boldsymbol{B}}{\mu_0} \cdot (\nabla_x \boldsymbol{v}) \boldsymbol{B} + \nabla_x \cdot (\mathbb{T}\boldsymbol{v}) \\ &= \left(p + \frac{\boldsymbol{B}^2}{2\mu_0}\right) \nabla_x \cdot \boldsymbol{v} + \mathbb{T} : \nabla_x \boldsymbol{v} - \frac{\boldsymbol{B}}{\mu_0} \cdot (\nabla_x \boldsymbol{v}) \boldsymbol{B}. \end{aligned}$$

Here, we have used the identity $\nabla_x(\mathbb{T}\boldsymbol{v}) = \boldsymbol{v} \cdot \nabla_x \cdot \mathbb{T}^t + \mathbb{T}^t : \nabla_x \boldsymbol{v}$, knowing that $\mathbb{T}^t = \mathbb{T}$. Now, recalling that the magnetic stress tensor reads

$$\mathbb{T} = -\left(p + \frac{\boldsymbol{B}^2}{2\mu_0}\right) \mathbb{I} + \frac{\boldsymbol{B} \otimes \boldsymbol{B}}{\mu_0},$$

we deduce that

$$\mathbb{T} : \nabla_x \boldsymbol{v} = \mathrm{tr}\,(\mathbb{T}(\nabla_x \boldsymbol{v})) = -\left(p + \frac{\boldsymbol{B}^2}{2\mu_0}\right) \nabla_x \cdot \boldsymbol{v} + \frac{1}{\mu_0} (\nabla_x \boldsymbol{v}) \boldsymbol{B} \cdot \boldsymbol{B},$$

since $\mathrm{tr}\,(\boldsymbol{u} \otimes \boldsymbol{w}) = \boldsymbol{u} \cdot \boldsymbol{w}$. Finally, the updated Lagrangian form of the entropy balance boils down to

$$\rho\theta \frac{\mathrm{d}\eta}{\mathrm{d}t} = 0. \tag{27}$$

This shows that entropy is conserved for smooth flows, while for non-smooth ones we prescribe the entropy inequality

$$\rho\theta \frac{\mathrm{d}\eta}{\mathrm{d}t} \geq 0, \tag{28}$$

to select the physically admissible shock waves.

3.5 Summary of the MHD system written under updated Lagrangian form

The system of MHD equations written under updated Lagrangian form reads

$$\begin{aligned}
&\rho\frac{\mathrm{d}\tau}{\mathrm{d}t} - \nabla_x \cdot \boldsymbol{v} = 0,\\
&\rho\frac{\mathrm{d}\boldsymbol{v}}{\mathrm{d}t} - \nabla_x \cdot \mathbb{T} = \boldsymbol{0},\\
&\rho\frac{\mathrm{d}E}{\mathrm{d}t} - \nabla_x \cdot (\mathbb{T}\boldsymbol{v}) = 0,\\
&\rho\theta\frac{\mathrm{d}\eta}{\mathrm{d}t} \geq 0.
\end{aligned}$$

The thermodynamic closure of this system is ensured by the complete EOS (7) and the magnetic stress tensor $\mathbb{T}$ reads

$$\mathbb{T} = -P_t\mathbb{I}_\mathrm{d} + \frac{\boldsymbol{B}\otimes\boldsymbol{B}}{\mu_0},$$

where the total pressure (2) is the summation of the thermodynamic pressure and the magnetic pressure. The magnetic field is expressed in terms of the deformation gradient $\mathbb{F}$ through (24)

$$\boldsymbol{B}(\boldsymbol{x},t) = J^{-1}(\boldsymbol{X},t)\mathbb{F}(\boldsymbol{X},t)\boldsymbol{B}^0(\boldsymbol{X}),$$

and we have shown in Section 3.3 that this expression is compatible with the involutive constraint, *i.e.* $\nabla_x \cdot \boldsymbol{B} = 0$, provided that $\mathbb{F}$ satisfies the GCL (17)

$$\frac{\mathrm{d}\mathbb{F}}{\mathrm{d}t} - (\nabla_x\boldsymbol{v})\mathbb{F} = 0.$$

This ends the presentation of the governing equations, and the next section presents the spatial discretization.

4 Finite Volume discretization

Let $\omega(t)$ be the computational domain at time $t > 0$. It is a subset of the three-dimensional space whose boundary surface $\partial\omega(t)$ is characterized by the outward pointing unit normal vector $\boldsymbol{n}$.

4.1 Grid and geometrical notations

We re-use the notations already introduced in [27, 30, 31, 36, 37]. At time $t > 0$, the computational domain $\omega(t)$ is paved by means of a set of non-overlapping simplicial cells. We denote by N_E the total number of elements/cells in the domain and a cell is referred to with label c, that is $\omega_c(t)$.

We also refer to a vertex/point with index p. Moreover the set of points of a cell is denoted by $\mathcal{P}(c)$ and the set of cells sharing a given point p is $\mathcal{C}(p)$. Next, the set of the faces of a cell is $\mathcal{F}(c)$ and the set of faces sharing a node p is $\mathcal{F}(p)$.

For any discrete time t^n, $n \in \mathbb{N}$, the union of all elements $\omega_c^n := \omega_c(t^n)$ paving $\omega(t^n)$ is called the *current mesh configuration* $\mathcal{T}_\omega^n$ of the domain

$$\mathcal{T}_\omega^n = \bigcup_{c=1}^{N_E} \omega_c^n. \tag{29}$$

Each control volume defined in the *physical* space $\boldsymbol{x} = (x, y, z)$ can be mapped onto a reference element ω_e in the reference coordinate system $\boldsymbol{\xi} = (\xi, \eta, \zeta)$ in 3D, see figure 2. Observing that any polyhedral cell can be split into tetrahedra, as such the method developed in this work is readily applicable on grids made of polyhedra.

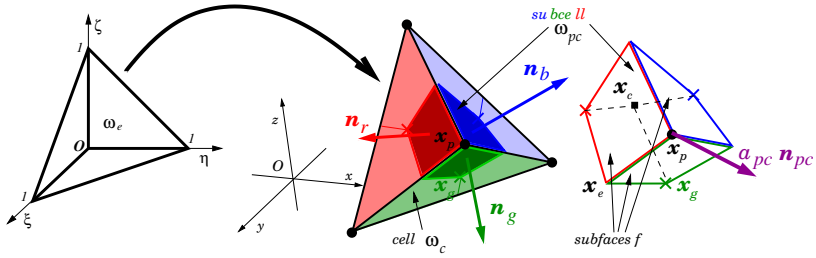

Fig. 2 Left: Reference simplicial element ω_e in coordinates $\boldsymbol{\xi} = (\xi, \eta, \zeta)$. Right: cell ω_c, sub-cell ω_{pc}, geometrical entities and outward pointing normals $\boldsymbol{n}$ to each sub-face $f \in \mathcal{SF}(pc)$ of sub-cell ω_{pc}.

The measure of the volume of the cell $\omega_c(t)$ is denoted by $|\omega_c(t)|$. The cell center, $\boldsymbol{x}_c$, corresponds to its centroid, that is

$$\boldsymbol{x}_c = \frac{1}{|\omega_c(t)|} \int_{\omega_c(t)} \boldsymbol{x} \, \mathrm{d}v.$$

The center of a face f is the iso-barycenter of the points defining the face

$$\boldsymbol{x}_f = \frac{1}{|\mathcal{P}(f)|} \sum_{p \in \mathcal{P}(f)} \boldsymbol{x}_p,$$

where $|\mathcal{S}|$ denotes the cardinal of any set $\mathcal{S}$.

Given a cell c and a point p we define a unique object called sub-cell, referred to with double index pc. The sub-cell ω_{pc} is the hexahedron whose vertices are the cell centroid $\boldsymbol{x}_c$, the point $\boldsymbol{x}_p$ and the face centroids $\boldsymbol{x}_f$ of the 3 faces $f \in \mathcal{F}(c)$ impinging at point p and the edge midpoints of the 3 edges

impinging at point p, see figure 2. In addition, each triangular face $f \in \mathcal{F}(c)$ is partitioned into 3 sub-faces. For instance, the sub-face attached to point p is the quadrangle whose vertices are p, the face centroid and the edge midpoints of the 2 edges impinging at p. The set of sub-faces of ω_c attached to point p is denoted $\mathcal{SF}(pc)$ and thus $\mathcal{SF}(pc) = \partial\omega_c \cap \partial\omega_{pc}$. Each sub-face $f \in \mathcal{SF}(pc)$ is assigned a unique outward pointing unit normal $\boldsymbol{n}_f$ and surface $a_f > 0$.

In the Lagrangian framework the cell mass m_c is constant with respect to time and defined by

$$m_c = \int_{\Omega_c} \rho^0(\boldsymbol{X})\,\mathrm{d}V = \int_{\omega_c} \rho(\boldsymbol{x}, t)\,\mathrm{d}v,$$

where Ω_c denotes the cell in the initial configuration and $\rho^0(\boldsymbol{X}) > 0$ is the initial density distribution.

The cell volume might be expressed in terms of its vertices location, that is

$$|\omega_c(t)| = \left|\omega_c\left(\boldsymbol{x}_1(t), \cdots, \boldsymbol{x}_{|\mathcal{P}(c)|}(t)\right)\right|.$$

Thus, applying the chain rule of composed derivative, the time rate of change of the cell volume writes

$$\frac{\mathrm{d}|\omega_c(t)|}{\mathrm{d}t} = \sum_{p\in\mathcal{P}(c)} \frac{\partial|\omega_c|}{\partial\boldsymbol{x}_p} \cdot \frac{\mathrm{d}\boldsymbol{x}_p}{\mathrm{d}t}. \tag{30}$$

This equation allows us to introduce the fundamental geometrical object

$$a_{pc}\boldsymbol{n}_{pc} = \frac{\partial|\omega_c|}{\partial\boldsymbol{x}_p}, \tag{31}$$

known as the corner normal vector. It has been already defined in the context of Lagrangian hydrodynamics, refer for instance to [37]. Here, a_{pc} represents a $(\mathrm{d}-1)$-measure (length in 2D, area in 3D) and $\boldsymbol{n}_{pc}$ is a unit outward pointing vector. Some algebraic manipulations allows to show that the corner normal vector is nothing but the summation of all the outward normals to the sub-faces attached to the cell corner pc

$$\sum_{f\in\mathcal{SF}(pc)} a_{pcf}\boldsymbol{n}_{pcf} = a_{pc}\boldsymbol{n}_{pc}, \tag{32}$$

where for any sub-face $f \in \mathcal{SF}(pc)$, a_{pcf} denotes its measure and $\boldsymbol{n}_{pcf}$ its unit outward normal. Moreover, the cell ω_c being a closed contour, the set of its corner normal vectors satisfies the fundamental geometrical identity

$$\sum_{p\in\mathcal{P}(c)} a_{pc}\boldsymbol{n}_{pc} = \boldsymbol{0}. \tag{33}$$

Let us point out that the corner normal vector relative to the initial Lagrangian cell, Ω_c, is similarly defined by

$$A_{pc}\boldsymbol{N}_{pc} = \frac{\partial|\Omega_c|}{\partial \boldsymbol{X}_p}. \tag{34}$$

4.2 Discrete velocity gradient operator

This paragraph aims at presenting a FV approximation of the velocity gradient for the updated Lagrangian representation. This operator is of great importance for deriving moving grid discretization of Lagrangian hydrodynamics, see for instance [31, 36]. The resulting discrete velocity gradient operator shall be useful for the space discretization of the Geometric Conservation Law which governs the time rate of change of the deformation gradient. Application of the divergence theorem leads to write the updated Lagrangian cell-centered velocity gradient operator

$$\mathbb{L}_c(\boldsymbol{v}) = \frac{1}{|\omega_c|}\int_{\partial\Omega_c} \boldsymbol{v}\otimes\boldsymbol{n}\,\mathrm{d}s.$$

Let us note that the velocity field is defined by its values at the cell nodes denoted by $\boldsymbol{v}_p = \boldsymbol{v}(\boldsymbol{x}_p)$. Now, approximating the foregoing integrals by means of the corner normal vectors (31) and the point-wise velocity field we arrive at the definition of the discrete velocity gradient operator

$$\mathbb{L}_c(\boldsymbol{v}) = \frac{1}{|\omega_c|}\sum_{p\in\mathcal{P}(c)} a_{pc}\boldsymbol{v}_p\otimes\boldsymbol{n}_p. \tag{35}$$

This discrete gradient operator is exact for affine velocity fields. This property relies on the geometrical identities (33) and

$$\sum_{p\in\mathcal{P}(c)} a_{pc}\boldsymbol{x}_p\otimes\boldsymbol{n}_{pc} = |\omega_c|\mathbb{I}_{\mathrm{d}}.$$

The interested reader might refer for instance to [38] for finding the demonstration of this result.

We end up presenting an important by-product of the discrete Eulerian velocity gradient operator. Taking the trace of (35) leads to

$$\mathrm{tr}\,[\mathbb{L}_c(\boldsymbol{v})] = \frac{1}{|\omega_c|}\sum_{p\in\mathcal{P}(c)} a_{pc}\boldsymbol{v}_p\cdot\boldsymbol{n}_{pc}.$$

This is nothing but the discrete cell-centered divergence operator. Finally, combining the definition of the Eulerian corner normal vector (31) and the discrete divergence operator leads to rewrite the time rate of change of the cell

volume as follows

$$\frac{1}{|\omega_c|}\frac{\mathrm{d}|\omega_c|}{\mathrm{d}t} = \mathrm{tr}\left[\mathbb{L}_c(\boldsymbol{v})\right] = \frac{1}{|\omega_c|}\sum_{p\in\mathcal{P}(c)} a_{pc}\boldsymbol{v}_p\cdot\boldsymbol{n}_{pc}. \tag{36}$$

Let us note that this equation has been obtained assuming that the nodal velocity is linked to the discrete trajectory equation

$$\frac{d\boldsymbol{x}_p}{dt} = \boldsymbol{v}_p,\ \boldsymbol{x}_p(0) = \boldsymbol{X}_p, \tag{37}$$

where $\boldsymbol{X}_p$ is the initial location of point p.

4.3 Magnetic field computation from the GCL: the link with hyperelasticity

We have derived a Finite Volume discretization for updated Lagrangian hyperelasticity [30] which relies on a compatible spatial discretization of the GCL. This compatibility stems from the care with which the deformation gradient equation (17) has been discretized employing the discrete velocity gradient operator (35)

$$\frac{\mathrm{d}\mathbb{F}_c}{\mathrm{d}t} - \mathbb{L}_c\mathbb{F}_c = 0, \tag{38}$$

where the discrete velocity gradient operator reads

$$\mathbb{L}_c = \frac{1}{|\omega_c|}\sum_{p\in\mathcal{P}(c)} a_{pcf}\left(\boldsymbol{v}_p\otimes\boldsymbol{n}_{pc}\right).$$

Knowing the cell-centered deformation gradient $\mathbb{F}_c$ we are now in position to compute the cell-centered magnetic field applying the analytical formula (24) and we obtain

$$\frac{\boldsymbol{B}_c}{\rho_c} = \mathbb{F}_c\frac{\boldsymbol{B}_c^0}{\rho_c^0}. \tag{39}$$

We point out that our updated Lagrangian FV discretization of MHD is simply a byproduct of our previous updated Lagrangian FV discretization of hyperelasticity. Gathering the foregoing results, we derive the semi-discrete equation satisfied by $\boldsymbol{B}_c$, which shall be useful to compute the cell entropy balance. Multiplying (39) by m_c, taking its time derivative and utilizing (38) yields

$$m_c\frac{\mathrm{d}}{\mathrm{d}t}\left(\frac{\boldsymbol{B}_c}{\rho_c}\right) - \left(\sum_{p\in\mathcal{P}(c)} a_{pc}\boldsymbol{v}_p\otimes\boldsymbol{n}_{pc}\right)\boldsymbol{B}_c = \boldsymbol{0}. \tag{40}$$

4.4 The discrete compatibility with the involution constraint for the magnetic field

The aim of this paragraph is to show in what sense the involution constraint is satisfied for the magnetic field. To this end, we have to define a discrete divergence operator to evaluate the divergence of the magnetic field at the discrete level. Since, the magnetic field is cell-centered, we choose to define a discrete divergence operator at the node, that is over the dual cell ω_p, which is constructed collecting the sub-cells sharing node p

$$\omega_p = \bigcup_{c\in\mathcal{C}(p)} \omega_{pc}, \tag{41}$$

where $\mathcal{C}(p)$ is the set of cells sharing node p. The discrete divergence of the magnetic field over the dual cell ω_p is defined by

$$\mathrm{DIV}_p(\boldsymbol{B}) = -\frac{1}{|\omega_p|}\sum_{c\in\mathcal{C}(p)} a_{pc}\boldsymbol{B}_c\cdot\boldsymbol{n}_{pc}. \tag{42}$$

This discrete divergence operator has been defined in a similar manner to the discrete gradient operator used in staggered grid Lagrangian hydrodynamics, refer for instance to [31]. Now, replacing the current $\boldsymbol{B}$ by its analytical expression (39) in the foregoing equation leads to

$$\begin{aligned}\mathrm{DIV}_p(\boldsymbol{B}) &= -\frac{1}{|\omega_p|}\sum_{c\in\mathcal{C}(p)} a_{pc}\frac{\rho_c}{\rho_c^0}\mathbb{F}_c\boldsymbol{B}_c^0\cdot\boldsymbol{n}_{pc},\\ &= -\frac{1}{|\omega_p|}\sum_{c\in\mathcal{C}(p)} J_c^{-1}\mathbb{F}_c^t a_{pc}\boldsymbol{n}_{pc}\cdot\boldsymbol{B}_c^0,\end{aligned} \tag{43}$$

where $\rho_c J_c = \rho_c^0$ thanks to the mass conservation. The discretization of the GCL introduced for hyperelasticity in [30] is fully compatible in the sense that the following property holds

$$a_c\boldsymbol{n}_{pc} = J_c\mathbb{F}_c^{-t}A_{pc}\boldsymbol{N}_{pc}, \tag{44}$$

where $A_{pc}\boldsymbol{N}_{pc}$ is the corner normal (34) related to the initial grid. Let us point out that this fundamental property only holds for simplicial grids since for a simplex the corner normal vector is nothing but the gradient of the finite element basis function attached to the node under consideration. We also observe that (44) is the discrete counterpart of the Nanson formula (18) which allows to express the Eulerian surface element in terms of its Lagrangian counterpart. Finally, substituting the discrete Nanson formula (44) into (43) we arrive at

$$\mathrm{DIV}_p(\boldsymbol{B}) = -\frac{1}{|\omega_p|}\sum_{c\in\mathcal{C}(p)} A_{pc}\boldsymbol{N}_{pc}\cdot\boldsymbol{B}_c^0.$$

Employing the discrete divergence operator defined over the dual cell Ω_p of the initial grid leads to express the discrete divergence of the current magnetic field in terms of the discrete divergence of the initial magnetic field as follows

$$\mathrm{DIV}_p(\boldsymbol{B}) = \frac{|\Omega_p|}{|\omega_p|}\mathrm{DIV}_p(\boldsymbol{B}^0). \tag{45}$$

The compatible spatial discretization of the GCL employed here, and borrowed from our previous work on Lagrangian hyperelasticity [30], provides us an analytical expression of the cell-centered magnetic field (39), wich is divergence preserving. Mainly, the divergence of the current magnetic field is expressed in terms of the divergence of the initial magnetic field through the discrete counterpart of the Piola formula (19). Therefore, if the initial cell-centered magnetic field is divergence free, the current magnetic field is also divergence free. This means that our spatial discretization is compatible with the involution constraint attached to the magnetic field. We recall that this fundamental property, which relies on the compatible discretization of the corner normal, is valid only for simplicial grids.

4.5 Spatial discretization of the conservation laws

4.5.1 The semi-discrete Finite Volume scheme

For any physical quantity $\varphi = \varphi(\boldsymbol{x}, t)$ we define its mass-averaged value over ω_c by

$$\varphi_c(t) = \frac{1}{m_c}\int_{\omega_c} \rho\varphi \,\mathrm{d}v, \tag{46}$$

where m_c is the constant mass of the Lagrangian cell ω_c. Integrating the MHD conservation laws (21a), (21b) and (21c) over ω_c leads to

$$m_c\frac{\mathrm{d}\tau_c}{\mathrm{d}t} - \int_{\partial\omega_c} \boldsymbol{v}\cdot\boldsymbol{n}\,\mathrm{d}s = 0, \tag{47a}$$

$$m_c\frac{\mathrm{d}\boldsymbol{v}_c}{\mathrm{d}t} - \int_{\partial\omega_c} \mathbb{T}\boldsymbol{n}\,\mathrm{d}s = \boldsymbol{0}, \tag{47b}$$

$$m_c\frac{\mathrm{d}E_c}{\mathrm{d}t} - \int_{\partial\omega_c} \mathbb{T}\boldsymbol{n}\cdot\boldsymbol{v}\,\mathrm{d}s = 0. \tag{47c}$$

Here, we have made use of the divergence theorem and we have also applied the following form of the Reynolds transport formula

$$\int_{\omega_c(t)} \rho\frac{d\varphi}{dt}\mathrm{d}v = \frac{d}{dt}\int_{\omega_c(t)} \rho\varphi\,\mathrm{d}v.$$

The spatial discretization of the volume conservation equation is classical: The surface integral in (47a) is approximated using the discrete divergence operator

introduced in section 4.2 which yields

$$m_c \frac{\mathrm{d}\tau_c}{\mathrm{d}t} - \sum_{p\in\mathcal{P}(c)} a_{pc}\boldsymbol{v}_p \cdot \boldsymbol{n}_{pc} = 0.$$

This ensures that the semi-discrete volume conservation equation is compatible with the GCL since $m_c\tau_c = |\omega_c|$ and thanks to (36).

Observing that the contour of ω_c might be split by means of the sub-cell contours as follows

$$\partial\omega_c = \bigcup_{p\in\mathcal{P}(c)} \partial\omega_c \cap \partial\omega_{pc},$$

the surface integral at the left hand-side of the momentum equation (47b) rewrites

$$\int_{\partial\omega_c} \mathbb{T}\boldsymbol{n}\,\mathrm{d}s = \sum_{p\in\mathcal{P}(c)} \int_{\partial\omega_c\cap\partial\omega_{pc}} \mathbb{T}\boldsymbol{n}\,\mathrm{d}s.$$

Defining the sub-face force, $\boldsymbol{F}_{pcf}$, as the traction force attached to sub-face f at corner pc

$$a_{pcf}\boldsymbol{F}_{pcf} = \int_{f\in\mathcal{SF}} \mathbb{T}\boldsymbol{n}\,\mathrm{d}s, \tag{48}$$

leads us to rewrite the surface integral in the momentum equation

$$\int_{\partial\omega_c} \mathbb{T}\boldsymbol{n}\,\mathrm{d}s = \sum_{p\in\mathcal{P}(c)} \sum_{f\in\mathcal{SF}(pc)} a_{pcf}\boldsymbol{F}_{pcf}.$$

Similarly, the surface integral in (47c) is approximated as

$$\int_{\partial\omega_c} \mathbb{T}\boldsymbol{n}\cdot\boldsymbol{v}\,\mathrm{d}s = \sum_{p\in\mathcal{P}(c)} \sum_{f\in\mathcal{SF}(pc)} a_{pcf}\boldsymbol{F}_{pcf}\cdot\boldsymbol{v}_p.$$

Finally, gathering the foregoing results system (47) turns into

$$m_c \frac{\mathrm{d}\tau_c}{\mathrm{d}t} - \sum_{p\in\mathcal{P}(c)} a_{pc}\boldsymbol{v}_p \cdot \boldsymbol{n}_{pc} = 0, \tag{49a}$$

$$m_c \frac{\mathrm{d}\boldsymbol{v}_c}{\mathrm{d}t} - \sum_{p\in\mathcal{P}(c)} \sum_{f\in\mathcal{SF}(pc)} a_{pcf}\boldsymbol{F}_{pcf} = \boldsymbol{0}, \tag{49b}$$

$$m_c \frac{\mathrm{d}E_c}{\mathrm{d}t} - \sum_{p\in\mathcal{P}(c)} \sum_{f\in\mathcal{SF}(pc)} a_{pcf}\boldsymbol{F}_{pcf}\cdot\boldsymbol{v}_p = 0. \tag{49c}$$

This system of semi-discrete conservation laws is supplemented with the trajectory equation (37). The remaining unknowns are the node velocity $\boldsymbol{v}_p$ and the sub-face traction force $\boldsymbol{F}_{pcf}$. We shall determine them invoking

- The entropy stability within cell ω_c;

- The conservation of total energy and momentum.

The sub-face force $\boldsymbol{F}_{pcf}$ expression in terms of the node velocity stems from the first requirement and the second one provides a linear system at each node satisfied by the node velocity.

4.5.2 Sub-face force expression to satisfy a local semi-discrete entropy inequality

We compute the local entropy production within cell ω_c induced by the semi-discrete scheme (49). The MHD Gibbs relation (12) reads

$$\theta \mathrm{d}\eta = P_t \mathrm{d}\tau - \boldsymbol{v} \cdot \mathrm{d}\boldsymbol{v} - \frac{\boldsymbol{B}}{\mu_0} \mathrm{d}\left(\frac{\boldsymbol{B}}{\rho}\right) + \mathrm{d}E,$$

where $P_t = p + \dfrac{\boldsymbol{B}^2}{2\mu_0}$ is the total pressure.

First, subtracting the kinetic energy to the total energy equation (49c) we get

$$m_c \frac{\mathrm{d}}{\mathrm{d}t}\left(E_c - \frac{1}{2}\boldsymbol{v}_c^2\right) - \sum_{p\in\mathcal{P}(c)} \sum_{f\in\mathcal{SF}(pc)} a_{pcf} \boldsymbol{F}_{pcf} \cdot (\boldsymbol{v}_p - \boldsymbol{v}_c) = 0. \tag{50}$$

Next, multiplying (49a) by P_t, and, further substituting (32) yields

$$m_c P_{t,c} \frac{\mathrm{d}\tau_c}{\mathrm{d}t} - \sum_{p\in\mathcal{P}(c)} \sum_{f\in\mathcal{SF}(pc)} a_{pcf} P_{t,c} \boldsymbol{n}_{pcf} \cdot (\boldsymbol{v}_p - \boldsymbol{v}_c) = 0. \tag{51}$$

Dot-multiplying (40) by $\frac{\boldsymbol{B}_c}{\mu_0}$ leads to

$$-\frac{\boldsymbol{B}_c}{\mu_0} \cdot \frac{\mathrm{d}}{\mathrm{d}t}\left(\frac{\boldsymbol{B}_c}{\rho_0}\right) + \sum_{p\in\mathcal{P}(c)} \sum_{f\in\mathcal{SF}(pc)} a_{pcf} \left(\boldsymbol{v}_p \otimes \boldsymbol{n}_{pcf}\right) \boldsymbol{B}_c \cdot \frac{\boldsymbol{B}_c}{\mu_0} = 0. \tag{52}$$

Observing that

$$\left(\boldsymbol{v}_p \otimes \boldsymbol{n}_{pcf}\right) \boldsymbol{B}_c \cdot \frac{\boldsymbol{B}_c}{\mu_0} = \boldsymbol{v}_p \cdot \left(\boldsymbol{B}_c \cdot \boldsymbol{n}_{pcf}\right) \frac{\boldsymbol{B}_c}{\mu_0} = \boldsymbol{v}_p \cdot \left(\frac{\boldsymbol{B}_c \otimes \boldsymbol{B}_c}{\mu_0}\right) \boldsymbol{n}_{pcf},$$

then (52) becomes

$$-\frac{\boldsymbol{B}_c}{\mu_0} \cdot \frac{\mathrm{d}}{\mathrm{d}t}\left(\frac{\boldsymbol{B}_c}{\rho_0}\right) + \sum_{p\in\mathcal{P}(c)} \sum_{f\in\mathcal{SF}(pc)} a_{pcf} \left(\frac{\boldsymbol{B}_c \otimes \boldsymbol{B}_c}{\mu_0}\right) \boldsymbol{n}_{pcf} \cdot (\boldsymbol{v}_p - \boldsymbol{v}_c) = 0. \tag{53}$$

Finally summing (50), (51), and (53) we arrive at

$$m_c \theta_c \frac{\mathrm{d}\eta_c}{\mathrm{d}t} = \sum_{p\in\mathcal{P}(c)} \sum_{f\in\mathcal{SF}(pc)} a_{pcf} \left(\boldsymbol{F}_{pcf} - \mathbb{T}_c \boldsymbol{n}_{pcf}\right) \cdot (\boldsymbol{v}_p - \boldsymbol{v}_c), \tag{54}$$

where $\mathbb{T}_c$ is the cell-centered value of the stress tensor which writes

$$\mathbb{T}_c = -\left(p_c + \frac{\boldsymbol{B}_c^2}{2\mu_0}\right)\mathbb{I}_\mathrm{d} + \left(\frac{\boldsymbol{B}_c \otimes \boldsymbol{B}_c}{\mu_0}\right). \tag{55}$$

We ensure a positive entropy production provided that the traction force writes under the form

$$\boldsymbol{F}_{pcf} = \mathbb{T}_c \boldsymbol{n}_{pcf} + \mathbf{M}_{pcf}(\boldsymbol{v}_p - \boldsymbol{v}_c), \tag{56}$$

where $\mathbf{M}_{pcf}$ has to be a positive definite $\mathrm{d} \times \mathrm{d}$ matrix attached to the sub-face f of sub-cell pc and has the dimension of a mass density times a velocity. With this expression the entropy balance within cell ω_c reads

$$m_c \theta_c \frac{\mathrm{d}\eta_c}{\mathrm{d}t} = \sum_{p \in \mathcal{P}(c)} \sum_{f \in \mathcal{SF}(pc)} a_{pcf} \mathbf{M}_{pcf}(\boldsymbol{v}_p - \boldsymbol{v}_c) \cdot (\boldsymbol{v}_p - \boldsymbol{v}_c) \geq 0.$$

One possible choice to design $\mathbf{M}_{pcf}$, inspired by what has been done for Lagrangian gas dynamics [31] consists in setting

$$\mathbf{M}_{pcf} = z_{pcf}\left(\boldsymbol{n}_{pcf} \otimes \boldsymbol{n}_{pcf}\right). \tag{57}$$

Here, $z_{pcf} > 0$ is a generalized impedance defined by $z_{pcf} = \rho_c \alpha_{pcf}$, where the wave speed α_{pcf} is computed using the fast magnetoacoustic wave speed [1] to maximize the entropy production rate

$$\alpha_{pcf} = \alpha_c \left[\frac{1}{2}\left(1 + \frac{\boldsymbol{B}_c^2}{\mu_0}\frac{\tau_c}{\alpha_c}\right) + \sqrt{\frac{1}{4}\left(1 + \frac{\boldsymbol{B}_c^2}{\mu_0}\frac{\tau_c}{\alpha_c}\right)^2 - \frac{B_{\boldsymbol{n}_{pcf}}^2}{\mu_0}\frac{\tau_c}{\alpha_c}}\right]^{1/2}, \tag{58}$$

where $B_{\boldsymbol{n}_{pcf}} = \boldsymbol{B}_c \cdot \boldsymbol{n}_{pcf}$.

4.5.3 The nodal solver enforcing the conservation of total energy and momentum

Considering the expression of the sub-face force (56), the conservation of momentum and total energy does not hold automatically true as in classical FV methods for which the numerical fluxes are face-based ones. Here, we shall derive a node-based conservation condition for both total energy and momentum - the mass being trivially conserved in Lagrangian schemes. Ignoring the boundary conditions, the conservation of total energy over the computational grid is ensured if and only if

$$\sum_c m_c \frac{\mathrm{d}E_c}{\mathrm{d}t} = 0 \iff \sum_c \sum_{p \in \mathcal{P}(c)} \sum_{f \in \mathcal{SF}(pc)} a_{pcf} \boldsymbol{F}_{pcf} \cdot \boldsymbol{v}_p = 0$$

$$\iff \sum_{p} \left(\sum_{c \in \mathcal{C}(p)} \sum_{f \in \mathcal{SF}(pc)} a_{pcf} \boldsymbol{F}_{pcf} \right) \cdot \boldsymbol{v}_p = 0,$$

where $\mathcal{C}(p)$ is the set of cells surrounding node p. Since it must be true for all point velocity $\boldsymbol{v}_p$, it is equivalent to the vectorial node-based condition

$$\sum_{c \in \mathcal{C}(p)} \sum_{f \in \mathcal{SF}(pc)} a_{pcf} \boldsymbol{F}_{pcf} = \mathbf{0}. \tag{59}$$

Substituting $\boldsymbol{F}_{pcf}$ by its expression (56) leads to the nodal solver

$$\mathbf{M}_p \boldsymbol{v}_p = \sum_{c \in \mathcal{C}(p)} \sum_{f \in \mathcal{SF}(pc)} -a_{pcf} \mathbb{T}_c \boldsymbol{n}_{pcf} + a_{pcf} \mathbf{M}_{pcf} \boldsymbol{v}_c, \tag{60}$$

where $\mathbf{M}_p = \sum_{c \in \mathcal{C}(p)} \sum_{f \in \mathcal{SF}(pc)} \mathbf{M}_{pcf}$ is always invertible since it is symmetric positive definite by construction, see the definition (57). Finally, the unique solution of the vectorial equation (60) provides us the nodal velocity.

5 Second-order ADER-based space-time discretization

We have developed a 3D cell-centered ADER-MOOD Finite Volume method for solving updated Lagrangian hyperelasticity model on unstructured grids [30]. This previous work constitutes the cornerstone on which we shall construct our Finite Volume space-time discretization of MHD by simply adapting the one developed in [30]. This construction relies on the analogy that we have put in evidence between Lagrangian hyperelasticity and Lagrangian ideal MHD which allows to express straightforwardly the magnetic field $\boldsymbol{B}$ in terms of the deformation gradient tensor $\mathbb{F}$.

In what follows, for the sake of self-consistency, we recall briefly the main steps needed for deriving the ADER-based space-time discretization of the MHD system, borrowing these results from our aforementioned work devoted to hyperelasticty.

5.1 Space-time discretization of physical conservation laws

The time interval $[0, T]$ is partitioned into sub-intervals $[t^n, t^{n+1}]$. Here, t^n is the current time, $t^{n+1} = t^n + \Delta t$ where Δt is the time step and $t = t^n + \alpha \Delta t$ for $\alpha \in [0, 1]$. For evaluating the magnitude of Δt we use a classical Courant-Friedrichs-Lewy (CFL) condition and a criterion to avoid a too large increase of cell volume in a single time step, refer for instance [39] knowing that its precise value shall be given in section 5.7. Knowing the physical variables and

the geometry at time t^n we start by computing the nodal velocity $\boldsymbol{v}_p^\star$ employing the nodal solver

$$\mathbf{M}_p \boldsymbol{v}_p^\star = \sum_{c\in\mathcal{C}(p)} \sum_{f\in\mathcal{SF}(pc)} -a_{pcf}^n \mathbb{T}_c^\star \boldsymbol{n}_{pcf} + a_{pcf}^n \mathbf{M}_{pcf} \boldsymbol{v}_c^\star, \tag{61}$$

where the * values on the right-hand side are obtained by space-time reconstructions detailed below. Furthermore, the discrete sub-face matrix $\mathbf{M}_{pc}$ and nodal matrix $\mathbf{M}_p$ read

$$\mathbf{M}_{pcf} = z_{pc}^\star \, \boldsymbol{n}_{pcf}^n \otimes \boldsymbol{n}_{pcf}^n, \qquad \mathbf{M}_p = \sum_{c\in\mathcal{C}(p)} \sum_{f\in\mathcal{SF}(pc)} \mathbf{M}_{pcf}. \tag{62}$$

The knowledge of the node velocity allows us to compute the sub-face force

$$\boldsymbol{F}_{pc}^\star = a_{pcf}^n \mathbb{T}_c^\star \boldsymbol{n}_{pcf}^n + \mathbf{M}_{pcf}(\boldsymbol{v}_p^\star - \boldsymbol{v}_c^\star). \tag{63}$$

Integrating the trajectory equation yields the updated node position

$$\boldsymbol{x}_p^{n+1} = \boldsymbol{x}_p^n + \Delta t \, \boldsymbol{v}_p^\star. \tag{64}$$

Then, it remains to perform the time explicit integration of the system of PDEs to arrive at the updated values of the physical state variables

$$\tau_c^{n+1} = \tau_c^n + \frac{\Delta t}{m_c} \sum_{p\in\mathcal{P}(c)} \widetilde{a_{pc}\boldsymbol{n}_{pc}} \cdot \boldsymbol{v}_p^\star, \tag{65a}$$

$$\boldsymbol{v}_c^{n+1} = \boldsymbol{v}_c^n + \frac{\Delta t}{m_c} \sum_{p\in\mathcal{P}(c)} \sum_{f\in\mathcal{SF}(pc)} \boldsymbol{F}_{pcf}^\star, \tag{65b}$$

$$E_c^{n+1} = E_c^n + \frac{\Delta t}{m_c} \sum_{p\in\mathcal{P}(c)} \sum_{f\in\mathcal{SF}(pc)} \boldsymbol{F}_{pcf}^\star \cdot \boldsymbol{v}_p^\star. \tag{65c}$$

The nodal velocity being given and constant during the time step, $\boldsymbol{x}_p$ is a linear function of time and thus the surface $\widetilde{l_{pc}\boldsymbol{n}_{pc}}$ is quadratic with respect to time. Therefore, the compatibility with the GCL at the discrete level requires an exact time integration of the volume flux in (65a), hence the Simpson quadrature rule

$$\begin{aligned}\widetilde{a_{pc}\boldsymbol{n}_{pc}} =& \frac{1}{\Delta t} \int_{t^n}^{t^{n+1}} a_{pc} \, \boldsymbol{n}_{pc} \, \mathrm{d}t \\ =& \frac{1}{6} a_{pc}^n \boldsymbol{n}_{pc}^n + \frac{2}{3} a_{pc}^{n+\frac{1}{2}} \boldsymbol{n}_{pc}^{n+\frac{1}{2}} + \frac{1}{6} a_{pc}^{n+1} \boldsymbol{n}_{pc}^{n+1} + O(\Delta t^3).\end{aligned} \tag{66}$$

For the first-order time discretization of (65b) and (65c) the geometrical and physical quantities are evaluated explicitly at time t^n. Recalling that for

the space discretization, the physical quantities are cell-centered. The second-order space discretization stems from a piece-wise linear reconstruction of the physical quantities within each cell. The second-order time discretization is achieved by means of the midpoint rule, thus we set $t^\star = t^{n+\frac{1}{2}} = \frac{1}{2}(t^n + t^{n+1})$. In this work following [27, 30, 40, 41], the second-order time discretization relies on the concept of the ADER (Arbitrary high order schemes using DERivatives) methodology. The ADER procedure computes high order space-time polynomials $\mathbf{q}_h(\boldsymbol{x}, t)$ defined in terms of a piece-wise linear space-time nodal basis functions $\theta(\boldsymbol{\xi}, \tau)$,

$$\mathbf{q}_h = \sum_{l=1}^{\mathcal{L}} \theta_l(\boldsymbol{\xi}, \tau) \widehat{\mathbf{q}}_{l,c}, \tag{67}$$

where $\widehat{\mathbf{q}}_{l,c}$ are the $\mathcal{L} = 2\mathcal{M}$ degrees of freedom with $\mathcal{M} = \mathrm{d}+1$. The space-time coordinate vector $(\boldsymbol{\xi}, \tau) = (\xi, \eta, \zeta, \tau)$ is defined in the spatial reference element given by the unit triangle/tetrahedron and in the reference time $\tau \in [0;\ 1]$ which maps the time step $[t^n;\ t^{n+1}]$ as $t = t^n + \tau\Delta t$, see [30].

5.2 Spatial reconstruction

First, a piece-wise linear spatial reconstruction is carried out providing a second order unlimited polynomial approximation of the current numerical solution, *i.e.* $\mathbf{q}_h(\boldsymbol{\xi}, 0)$. The limiting will be done *a posteriori* via the MOOD paradigm. A so-called reconstruction stencil $\mathcal{S}_c = \bigcup_{j=1}^{n_e} \omega^n_{m(j)}$ is needed, where $1 \le j \le n_e$ is a local index that counts the elements belonging to the stencil, while $m(j)$ maps the local index to the global element numbers. Notice that neither the stencil nor the element configuration is symmetric on unstructured meshes, thus, to avoid ill-conditioned reconstruction matrices, the stencil contains a total number of $n_e = \mathrm{d}\mathcal{M}$ elements made by the neighbor elements sharing at least one vertex with element ω^n_c. The reconstruction relies on integral conservation for each element $\omega^n_j \in \mathcal{S}_c$, that is

$$\forall \omega^n_j \in \mathcal{S}_c, \quad \frac{1}{|\omega^n_j|} \int_{\omega^n_j} \sum_{l=1}^{\mathcal{L}} \theta_l(\boldsymbol{\xi}, 0)\, \widehat{\mathbf{q}}_{l,c}\, \mathrm{d}v \simeq \mathbf{Q}^n_j,$$

$$\frac{1}{|\omega^n_c|} \int_{\omega^n_c} \sum_{l=1}^{\mathcal{M}} \theta_l(\boldsymbol{\xi}, 0)\, \widehat{\mathbf{q}}_{l,c}\, \mathrm{d}v = \mathbf{Q}^n_c,$$

where $\boldsymbol{Q}_c = (\tau_c, \boldsymbol{v}_c, E_c, \tau_c \boldsymbol{B}_c)$ is the vector of the cell-centered state variables. The foregoing system is classically solved using a constrained least squares technique [42].

5.3 Time reconstruction.

Once $\mathbf{q}_h(\boldsymbol{\xi},0)$ is known, the ADER methodology performs a local time evolution of the governing equations. To that aim, a weak formulation is derived by multiplying the PDE with a space-time test function $\theta_k(\boldsymbol{\xi},\tau)$ that is

$$\int_{t^n}^{t^{n+1}} \int_{\omega_c(t)} \theta_k(\boldsymbol{\xi},\tau) \left(\frac{\mathrm{d}\mathbf{q}_h}{\mathrm{d}t} - \frac{1}{\rho_h} \nabla \cdot \mathbb{G}(\mathbf{q}_h) \right) \mathrm{d}v \, \mathrm{d}t = 0, \tag{68a}$$

$$\int_{t^n}^{t^{n+1}} \int_{\omega_c(t)} \theta_k(\boldsymbol{\xi},\tau) \frac{\mathrm{d}\boldsymbol{x}}{\mathrm{d}t} \, \mathrm{d}v \, \mathrm{d}t = \int_{t^n}^{t^{n+1}} \int_{\omega_c(t)} \theta_k(\boldsymbol{\xi},\tau) \, \boldsymbol{v} \, \mathrm{d}v \, \mathrm{d}t, \tag{68b}$$

with the state vector $\mathbf{q}_h = (\tau, \boldsymbol{v}, e, \boldsymbol{B}\tau)_h$ and the flux tensor $\mathbb{G}(\mathbf{q}_h) = (\boldsymbol{v}, \mathbb{T}, \mathbb{T}\boldsymbol{v}, \boldsymbol{v}\boldsymbol{B})_h$. The trajectory equation (68b) is coupled with the evolution of the governing PDE (68a), and the local element geometry is defined by $\boldsymbol{x}_h$ which is expressed in terms of the space-time basis functions as $\boldsymbol{x}_h = \sum_{l=1}^{\mathcal{L}} \theta_l(\boldsymbol{\xi},\tau)\widehat{\boldsymbol{x}}_{l,c}$. The first $\mathcal{L}/2$ degrees of freedom are known, since they correspond to the spatial reconstruction polynomial $\mathbf{q}_h(\boldsymbol{\xi},0)$ and to the vertex coordinates of the cell ω_c at time t^n. The above nonlinear system (68) can be compactly written in matrix-vector notation and then solved iteratively up to convergence for both the numerical solution $\mathbf{q}_h$ and the local geometry configuration $\boldsymbol{x}_h$, to obtain the remaining unknown $\mathcal{L}/2$ expansion coefficients for $\tau > 0$. All the details can be found in [27, 42, 43]. The result of the ADER predictor is a continuous second order space-time polynomial for both the numerical solution and the element geometry, which easily allows to evaluate any physical or geometric quantity in the space-time control volume $\omega_c(t)$ for any $t \in [t^n;\ t^{n+1}]$. As a consequence, once the predictor is available, the sub-face forces and the node values in (65a)-(65c) are simply fed with the high order extrapolated values of the predictor, hence for any variable it holds $\mathbf{q}^\star(\boldsymbol{x}) = \mathbf{q}_h(\boldsymbol{x}, t^\star)$ for any space-time coordinate $(\boldsymbol{x}, t)$.

5.4 Space-time discretizations of the deformation gradient tensor and the magnetic field

Let us emphasize that in our unconventional approach the magnetic field discretization stems from the deformation gradient discretization through the use of the fundamental kinematic relation (39), which once time integrated yields

$$\boldsymbol{B}_c^{n+1} = \frac{\mathbb{F}_c^{n+1}}{\det(\mathbb{F}_c^{n+1})} \boldsymbol{B}_c^0. \tag{69}$$

Finally, we point out that the update of the cell-centered magnetic field simply results from the update of the cell-centered deformation gradient tensor $\mathbb{F}_c$

which is obtained through the semi-discrete updated Lagrangian version of the GCL (38) that is

$$\frac{\mathrm{d}\mathbb{F}_c}{\mathrm{d}t} - \mathbb{L}_c\mathbb{F}_c = 0,$$

where $\mathbb{L}_c$ is the discrete velocity gradient operator (35). It remains to propose a space-time discretization of the GCL which is fully compatible with the Lagrange-to-Euler mapping, *i.e.*, with the grid displacement. This has been already done in our previous work dedicated to hyperelasticy [30] and we recall here the main results. We construct the second-order time discretization of (38) employing the classical Crank-Nicholson integration scheme over the time interval $[t^n, t^{n+1}]$ which reads

$$\mathbb{F}_c^{n+1} - \mathbb{F}_c^n - \frac{\Delta t}{2}\mathbb{L}_c^{n+\frac{1}{2}}(\mathbb{F}_c^{n+1} + \mathbb{F}_c^n) = 0,$$

where $\mathbb{L}_c^{n+\frac{1}{2}}$ denotes the time-centered approximation of the discrete velocity gradient operator which acts over ω_c, that is given by

$$\mathbb{L}_c^{n+\frac{1}{2}} = \frac{1}{|\omega_c^{n+\frac{1}{2}}|}\sum_{p\in\mathcal{P}(c)} l_{pc}^{n+\frac{1}{2}}\boldsymbol{v}_p^{n+\frac{1}{2}} \otimes \boldsymbol{n}_{pc}^{n+\frac{1}{2}}.$$

Notice that the the node velocity $\boldsymbol{v}_p^{n+\frac{1}{2}}$ is computed using the nodal solver (61) fed with high-order vertex extrapolated data coming from the ADER predictor solution $\mathbf{q}_h$. The geometric quantities can also be evaluated at time $t^{n+\frac{1}{2}}$ after solving the trajectory equation (22) with the node velocity previously obtained.

Let us carry out the following Taylor expansion for $\Delta t \to 0$

$$\det\left(\mathbb{I}_\mathrm{d} - \frac{\Delta t}{2}\mathbb{L}_c^{n+\frac{1}{2}}\right) = 1 - \frac{\Delta t}{2}\mathrm{tr}(\mathbb{L}_c^{n+\frac{1}{2}}) + O(\Delta t^2).$$

Observing the right hand side of the foregoing equation it is clear that there exists $\Delta t > 0$ such that $\det\left(\mathbb{I}_\mathrm{d} - \frac{\Delta t}{2}\mathbb{L}_c^{n+\frac{1}{2}}\right) > 0$, and thus $\mathbb{I}_\mathrm{d} - \frac{\Delta t}{2}\mathbb{L}_c^{n+\frac{1}{2}}$ is invertible. Under this time step constraint the updated cell-centered value of the deformation gradient within cell ω_c reads

$$\mathbb{F}_c^{n+1} = \left(\mathbb{I}_\mathrm{d} - \frac{\Delta t}{2}\mathbb{L}_c^{n+\frac{1}{2}}\right)^{-1}\left(\mathbb{I}_\mathrm{d} + \frac{\Delta t}{2}\mathbb{L}_c^{n+\frac{1}{2}}\right)\mathbb{F}_c^n. \tag{70}$$

5.5 Limiting: *a posteriori* MOOD loop

Following [30] we adopt an *a posteriori* MOOD paradigm, see [27, 44]. The technique is *a posteriori* in the sense that we compute a solution at time t^{n+1}, and, then, determine if this candidate solution is acceptable, or not and some dissipation is needed. The candidate solution is first computed with a second-order accurate unlimited scheme using a centered reconstruction stencil. Then

a detection procedure determines the problematic cells for which the approximation does not respect some user-given criteria. For those cells the solution is locally recomputed with a lower-order but more robust scheme. A cascade of three schemes, each of them chosen to comply with one specific objective, is employed:

1. $\mathbb{P}_1$: *Accuracy* with the unlimited piece-wise linear polynomial reconstruction: maximal second-order of accuracy, possibly oscillating;
2. $\mathbb{P}_1^{\text{lim}}$: *Robustness* with the previous reconstruction supplemented with Barth-Jespersen (BJ) [45] slope limiter: between first- and second-order of accuracy, essentially-non-oscillatory;
3. $\mathbb{P}_0$: *Fail-safe* without any polynomial reconstruction: first-order of accuracy, fail-safe but overly dissipative.

The cascade is then $\mathbb{P}_1 \rightarrow \mathbb{P}_1^{\text{lim}} \rightarrow \mathbb{P}_0$. A cell which does not satisfy all detection criteria is recomputed with the next scheme in the cascade. This procedure, called the MOOD loop, is repeated until each cell satisfies all detection criteria or if the latest scheme of the cascade is selected. The process of dropping in the cascade is called *decrementing* and a numerical solution not yet valid is referred to as being a *candidate solution*. In the case of MHD $\mathbf{Q}_h^{\star,n+1}$ is physically admissible if it belongs to $\mathcal{A}_h = \{\mathbf{Q}_c = (\tau_c, \boldsymbol{v}_c, E_c, \boldsymbol{B}_c\tau_c) \text{ s.t. } \tau_c > 0,\ \varepsilon_c > 0,\ \theta_c > 0, \}$. Moreover to avoid spurious oscillations we also demand that the candidate density fulfills a Relaxed Discrete Maximum Principle (RDMP) that is

$$
\begin{aligned}
&-\delta_c^n + m_c^n \leq \rho_c^{\star,n+1} \leq M_c^n + \delta_c^n, \text{ where} \\
&\delta_c^n = \max(\delta_0, \delta_1 |M_c^n - m_c^n|), \\
&m_c^n = \min_{d\in\mathcal{V}_c}(\rho_d^n), \text{ and } M_c^n = \max_{d\in\mathcal{V}_c}(\rho_d^n).
\end{aligned} \tag{71}
$$

Here, $\mathcal{V}_c$ is the same neighborhood used to reconstruct the piece-wise polynomials. We fix $\delta_0 = 10^{-4}$ and $\delta_1 = 10^{-3}$. Any cell which does not belong to $\mathcal{A}_h$ or does not fulfill (71) is declared troubled, and, sent back to t^n along with its neighbors for their re-computation using the next scheme of the cascade. The MOOD loop always converges and produces an acceptable numerical solution, assuming that the parachute scheme does so. According to the cascade we will systematically monitor where the troubled/bad cells are located, hence also where the limited scheme (less than second-order accurate) does operate.

5.6 Internal consistency consideration

The internal consistency of the numerical scheme is related to its ability to maintain some mathematical equality at a reasonable level of accuracy during the simulation[1].

[1] Such a concern was for instance raised in [46] in the context of hydrodynamics solved by a staggered Lagrangian scheme where the cell volume can be computed either from the point coordinates or the PDE for the specific volume τ. The difference between these two "measures" was monitored to assess the internal consistency of the scheme.

The first of such equality is the link between the constant cell mass, the specific volume τ (or the density $\rho = 1/\tau$) and volume $|\omega|$: $m = \dfrac{|\omega|}{\tau}$. The discrete constant mass is computed initially from the initial specific volume in the cell as $m_c \equiv m_c^0 = \dfrac{|\omega_c^0|}{\tau_c^0}$. The primary variable is the specific volume: τ_c^{n+1} computed by (65a). The new position of the points $\boldsymbol{x}_p^{n+1}$ allows to deduce the cell volume $|\omega_c^{n+1}|$ as a secondary variable. However, we could also deduce the cell volume consistently with the PDE (49a) as being $\tau_c^{n+1} m_c$. Therefore, from a consistency point of view, we should monitor that the following equality holds

$$\epsilon_\omega = ||\omega_c^{n+1}| - \tau_c^{n+1} m_c|. \tag{72}$$

This constraint is nothing but the discrete version of the GCL which is fulfilled by construction for modern cell-centered Lagrangian schemes thanks to the exact integration of the geometry in (66).
Our Finite Volume formulation of updated Lagrangian MHD ensures that the divergence of the magnetic field at time $t > 0$ remains proportional to the divergence of the initial magnetic field, refer to Section 4.4 and (45). At the discrete level, the magnetic field is known by means of a piece-wise constant cell-centered representation. We propose to monitor the difference between the discrete divergence of the magnetic field at time $t = t^n$ and $t = 0$ to assess the internal consistency of the numerical method regarding the divergence preserving property. This corresponding measure is achieved by computing the indicator

$$|\nabla \cdot \boldsymbol{B}|_{h,\max}^n = \max_p |\mathrm{DIV}_p(\boldsymbol{B}^n) - \mathrm{DIV}_p(\boldsymbol{B}^0)|, \tag{73}$$

where $\mathrm{DIV}_p(\boldsymbol{B}^n)$ denotes the discrete divergence operator defined over the dual cell ω_p as follows

$$\mathrm{DIV}_p(\boldsymbol{B}^n) = -\frac{1}{|\omega_p^n|} \sum_{c \in \mathcal{C}(p)} a_{pc}^n \boldsymbol{n}_{pc}^n \cdot \boldsymbol{B}_c^n.$$

5.7 Time-step monitoring

The time step is monitored using the Lagrangian CFL condition [39]

$$\Delta t = \min\left(\Delta t_{\mathrm{volume}},\ \Delta t_{\mathrm{acoustic}},\ \Delta t_{\mathrm{increase}}\right), \tag{74}$$

where the different time steps in the foregoing formula are given by

$$\Delta t_{\mathrm{volume}} = C_v \min_c \left(\frac{|\omega_c^n|}{|\sum_{p \in \mathcal{P}(c)} a_{pc}^n \boldsymbol{n}_{pc}^n \cdot \boldsymbol{v}_p|} \right),$$

$$\Delta t_{\text{acoustic}} = C_{\text{CFL}} \min_c \left(\frac{L_c}{\alpha_c} \right), \ \Delta t_{\text{increase}} = C_i (t^n - t^{n-1}).$$

Here, L_c is the cell characteristics length (smallest diameter of the in-spheres), α_c is an estimation of the fast magnetoacoustic wave speed (58) and $\{C_v, C_{\text{CFL}}, C_i\} \in [0,1]^3$. The last constraint is designed to avoid a too large variation of Δt. Notice that the time step control must be suited for the parachute scheme to ensure the positivity of the cell volume and the internal energy. In our simulations we take $C_v = 0.2$, $C_i = 0.1$ and $C_{\text{CFL}} = 0.25$ otherwise noticed.

6 Numerical results

In the following we present a suite of numerical test problems which aims at validating the accuracy and the robustness of the novel Lagrangian ADER-MOOD (LAM) algorithm for the solution of the ideal MHD equations.

The magnetic permeability is assumed to be $\mu_0 = 1$ if not stated otherwise. Likewise, the second order version of the LAM scheme is used and the Courant number is set to $C_{\text{CFL}} = 0.25$. The error related to the discrete divergence of the magnetic field is also systematically monitored employing the indicator defined by (73) and (**??**).

The initial condition is typically given for each test case in terms of primitive variables, that is $\mathbf{V} = (\rho, u, v, w, p, B_x, B_y, B_z)$. The deformation gradient is always initialized with the identity matrix, hence $\mathbb{F} = \mathbb{I}_{\text{d}}$.

The cell order map is used to show those cells which undergo the limiting process. Specifically, we plot in blue unlimited cells and in red the limited ones.

6.1 Numerical convergence studies

The numerical convergence studies for the ideal MHD equations are carried out using a smooth MHD vortex problem firstly proposed in [47]. The initial computational domain is the square $\omega(0) = [0;\ 10] \times [0;\ 10]$ with periodic boundaries in all directions. The ratio of specific heats is $\gamma = 5/3$ and the magnetic permeability is set to $\mu_0 = 4\pi$. The initial condition is given again as a superposition of a constant flow plus some fluctuations:

$$\mathbf{V}(\boldsymbol{x}, 0) = (1 + \delta\rho, 1 + \delta u, 1 + \delta v, 0, 1 + \delta p, 1 + \delta B_x, 1 + \delta B_y, 0), \tag{75}$$

with the perturbations

$$\begin{pmatrix} \delta u \\ \delta v \\ \delta p \\ \delta B_x \\ \delta B_y \end{pmatrix} = \begin{pmatrix} \frac{\beta}{2\pi} e^{\frac{1}{2}(1-r^2)}(5-y) \\ \frac{\beta}{2\pi} e^{\frac{1}{2}(1-r^2)}(x-5) \\ \frac{1}{8\pi}\left(\frac{\alpha}{2\pi}\right)^2 (1-r^2) e^{(1-r^2)} - \frac{1}{2}\left(\frac{\beta}{2\pi}\right)^2 e^{(1-r^2)} \\ \frac{\alpha}{2\pi} e^{\frac{1}{2}(1-r^2)}(5-y) \\ \frac{\alpha}{2\pi} e^{\frac{1}{2}(1-r^2)}(x-5) \end{pmatrix}. \tag{76}$$

The parameters to determine the vortex strength are $\alpha = \sqrt{4\pi}$ and $\beta = 1$. The final time is $t_f = 0.1$ and the vortex is convected with velocity $\boldsymbol{v}_c = (1, 1)$. Figure 3 shows the evolution of the computational domain up to time $t = 2$ which is indeed convected according to $\boldsymbol{v}_c$, while maintaining a stationary solution for the flow variables, as visible for the magnitude of the magnetic field.

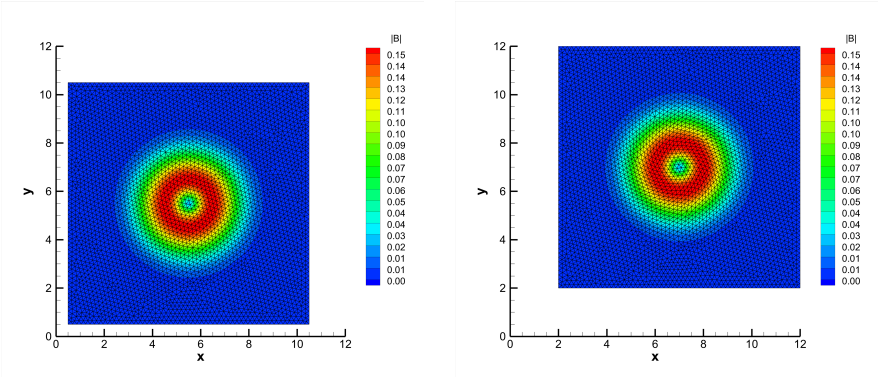

Fig. 3 MHD isentropic test for numerical convergence studies. Magnitude of the magnetic field and mesh configuration at time $t = 0.5$ (left) and $t = 2$ (right).

The exact solution $\mathbf{V}_e(\boldsymbol{x}, t)$ is then given by the initial condition $\mathbf{V}(\boldsymbol{x}, 0)$ shifted in space by $\boldsymbol{s} = \boldsymbol{v}_c t_f$ and the errors are measured in L_2 and L_∞ norms defined as

$$L_p = \left[\int_{\omega(t_f)} \left(\mathbf{V}_e(\boldsymbol{x}, t_f) - \mathbf{q}_h(\boldsymbol{x}, t_f) \right)^p \, d\boldsymbol{x} \right]^{1/p},$$
$$L_\infty = \max_{\omega(t_f)} \left| \mathbf{V}_e(\boldsymbol{x}, t_f) - \mathbf{q}_h(\boldsymbol{x}, t_f) \right|,$$

where $p = 2$ corresponds to the L_2 norm and $\mathbf{q}_h(\boldsymbol{x}, t_f)$ denotes the reconstructed solution at the final time of the simulation t_f. The mesh size $h(\omega(t_f))$ is taken to be the maximum diameter of the circumcircles of the triangles in the final domain $\omega(t_f)$. Tables 1 and 2 report the convergence studies for first and second order accurate LAM schemes, respectively. The formal order of accuracy is preserved in both space and time by performing the simulation on a sequence of successively refined triangular meshes. Furthermore, the second order version of the algorithm systematically achieves smaller errors for all variables and characteristic mesh sizes.

Finally, we also study the convergence of the magnetic field components for longer times and on finer meshes, and the results are reported in Table 3. The magnetic field equation contains also geometry information hence providing a good indicator for the convergence of the scheme, which is proven to be second

Table 1 Numerical convergence results for the ideal MHD equations using the *first order* Lagrangian ADER-MOOD (LAM) scheme. The errors are measured in L_2 and L_∞ norms and refer to the variables u (horizontal velocity), E (total energy) and B_y (magnetic field component in y direction) at time $t_f = 0.1$.

LAM $\mathcal{O}1$

$h(\omega(t_f))$	$L_2(u)$	$\mathcal{O}(u)$	$L_2(E)$	$\mathcal{O}(E)$	$L_2(B_y)$	$\mathcal{O}(B_y)$
5.53E-01	8.095E-02	-	1.162E-01	-	2.406E-01	-
2.93E-01	4.454E-02	0.94	6.317E-02	0.96	1.212E-01	1.08
2.05E-01	3.083E-02	1.03	4.378E-02	1.03	8.079E-02	1.14
1.50E-01	2.367E-02	0.84	3.343E-02	0.85	6.073E-02	0.90

$h(\omega(t_f))$	$L_\infty(u)$	$\mathcal{O}(u)$	$L_\infty(E)$	$\mathcal{O}(E)$	$L_\infty(B_y)$	$\mathcal{O}(B_y)$
5.53E-01	5.863E-02	-	7.887E-02	-	1.737E-01	-
2.93E-01	3.154E-02	0.98	4.755E-02	0.80	9.435E-02	0.96
2.05E-01	2.141E-02	1.09	3.209E-02	1.10	6.299E-02	1.13
1.50E-01	1.609E-02	0.90	2.465E-02	0.83	4.800E-02	0.86

Table 2 Numerical convergence results for the ideal MHD equations using the *second order* Lagrangian ADER-MOOD (LAM) scheme. The errors are measured in L_2 and L_∞ norms and refer to the variables u (horizontal velocity), E (total energy) and B_y (magnetic field component in y direction) at time $t_f = 0.1$.

LAM $\mathcal{O}2$

$h(\omega(t_f))$	$L_2(u)$	$\mathcal{O}(u)$	$L_2(E)$	$\mathcal{O}(E)$	$L_2(B_y)$	$\mathcal{O}(B_y)$
5.53E-01	2.242E-02	-	3.385E-02	-	6.237E-02	-
2.93E-01	5.038E-03	2.36	8.371E-03	2.21	1.578E-02	2.17
2.05E-01	2.099E-03	2.45	4.119E-03	1.99	7.017E-03	2.27
1.50E-01	1.170E-03	1.85	2.672E-03	1.37	4.025E-03	1.76

$h(\omega(t_f))$	$L_\infty(u)$	$\mathcal{O}(u)$	$L_\infty(E)$	$\mathcal{O}(E)$	$L_\infty(B_y)$	$\mathcal{O}(B_y)$
5.53E-01	1.663E-02	-	2.408E-02	-	3.702E-02	-
2.93E-01	3.529E-03	2.45	5.620E-03	2.30	1.032E-02	2.02
2.05E-01	1.412E-03	2.57	2.463E-03	2.31	4.651E-03	2.24
1.50E-01	7.666E-04	1.93	1.550E-03	1.47	2.622E-03	1.81

order accurate. Moreover, the solution in terms of errors is quite symmetric for both components of the magnetic field. For even longer times, the mesh distortion becomes too important and causes a degeneracy in the accuracy analysis.

6.2 MHD Taylor-Green vortex

The Taylor-Green vortex flow represents a steady-state solution of the incompressible Navier-Stokes equations. In [34, 48] this test case has been extended to compressible inviscid flows by means of an artificial source term in the energy equation which balances the mechanical forces induced by the

Table 3 Numerical convergence results for the ideal MHD equations using the *second order* Lagrangian ADER-MOOD (LAM) scheme for the magnetic field components B_x and B_y. The errors are measured in L_2 at time $t_f = 0.2$.

LAM $\mathcal{O}2$				
$h(\omega(t_f))$	$L_2(B_x)$	$\mathcal{O}(B_x)$	$L_2(B_y)$	$\mathcal{O}(B_y)$
5.53E-01	1.947E-02	-	1.972E-02	-
2.93E-01	4.944E-03	2.17	4.923E-03	2.19
2.05E-01	2.214E-03	2.25	2.220E-03	2.23
1.50E-01	1.289E-03	1.71	1.281E-03	1.74
1.22E-01	8.636E-04	1.92	8.684E-04	1.86
1.04E-01	6.424E-04	1.87	6.460E-04	1.87

fluid vorticity. Recently [49], a similar version of the problem for MHD fluids has been derived, which is the one adopted here. The computational domain is $\omega(0) = [0;\ 1]^2$ with wall boundary conditions imposed on every side. The ratio of specific heats is set to $\gamma = 5/3$ [49], and the initial condition is given in terms of primitive variables by

$$\boldsymbol{V}(\boldsymbol{x},0) = \begin{cases} 1 \\ \sin(\pi x)\cos(\pi y) \\ -\cos(\pi x)\sin(\pi y) \\ 0 \\ P(\boldsymbol{x}) \\ \beta\sqrt{\mu_0}\sin(\pi x)\cos(\pi y) \\ -\beta\cos(\pi x)\sin(\pi y) \\ 0 \end{cases}$$

The initial pressure field reads

$$P(\boldsymbol{x}) = 1 + \frac{1-\beta^2}{4}\left(\cos(2\pi x) + \cos(2\pi y)\right) - \frac{\beta^2(1-\beta^2)}{8}\left(\sin^2(\pi x)\cos^2(\pi y) + \cos^2(\pi x)\sin^2(\pi y)\right).$$

The parameter β prescribes the strength of the magnetic field over the hydrodynamic pressure field and we set $\beta = \frac{1}{2}$. To preserve a stationary solution, the following source term must be added to the energy equation:

$$S_e = \frac{\pi}{4(\gamma-1)}\left(\cos(3\pi x)\cos(\pi y) - \cos(\pi x)\cos(3\pi y)\right),$$

which is integrated using a midpoint rule in space and time over the moving control volumes. According to [34], the simulation is run until the final time $t_f = 0.1$, and a convergence study is performed. The results are collected in

Table 4 for first and second order schemes and the errors are measured in L_2 norm for the first component of the velocity and the magnetic field. The distribution of the pressure and magnitude of the velocity field are depicted in Figure 4, and the evolution of the divergence error is shown as well. We observe that the formal order of accuracy is captured by our novel schemes which can also maintain the solenoidal property of the magnetic field.

Table 4 Numerical convergence results for the ideal MHD equations using the first and second order Lagrangian ADER-MOOD (LAM) scheme solving the MHD Taylor-Green vortex problem. The errors are measured in L_2 norm and refer to the variables u (horizontal velocity) and B_x (magnetic field component in x direction) at time $t_f = 0.1$.

LAM $\mathcal{O}1$

$h(\omega(t_f))$	$L_2(u)$	$\mathcal{O}(u)$	$L_2(B_x)$	$\mathcal{O}(B_x)$
2.86E-02	7.232E-02	-	5.092E-03	-
1.47E-02	3.703E-02	1.00	3.208E-03	0.69
1.03E-02	2.477E-02	1.13	1.981E-03	1.35
7.97E-03	1.967E-02	0.91	1.513E-03	1.06

LAM $\mathcal{O}2$

$h(\omega(t_f))$	$L_2(u)$	$\mathcal{O}(u)$	$L_2(B_x)$	$\mathcal{O}(B_x)$
2.70E-02	9.863E-03	-	4.017E-03	-
1.48E-02	2.444E-03	2.31	2.298E-03	0.92
1.03E-02	1.081E-03	2.27	1.187E-03	1.84
7.98E-03	6.797E-04	1.81	7.402E-04	1.84

6.3 MHD shock tube problems

In this section, the LAM schemes are applied to a set of Riemann problems of the ideal MHD equations taken from [50], which are typically used in the literature to assess conservation and robustness of a novel numerical scheme [25, 51–53]. The computational domain is the rectangular box $\omega(0) = [-0.5;\ 0.5] \times [-0.05;\ 0.05]$ with periodic boundary conditions in $y-$direction and pressure boundaries in $x-$direction. The initial condition for a Riemann problem is given in terms of a left (L) and a right (R) state separated by a discontinuity located at $x_d = 0$. Table 5 contains the initial data for the eight Riemann problems considered in this section, as well as the final time of each simulation.

The domain is paved with a triangular mesh of characteristic size $h = 1/200$ and $h = 1/400$ for RP1-RP2 and RP4-RP8, respectively, that are coarser than the mesh resolutions adopted in the aforementioned references. Indeed, the Lagrangian design of the scheme allows a physical mesh refinement to automatically arise close to shocks while exactly solving contact discontinuities. The ratio of specific heats is $\gamma = 5/3$ for all cases. Although being one-dimensional

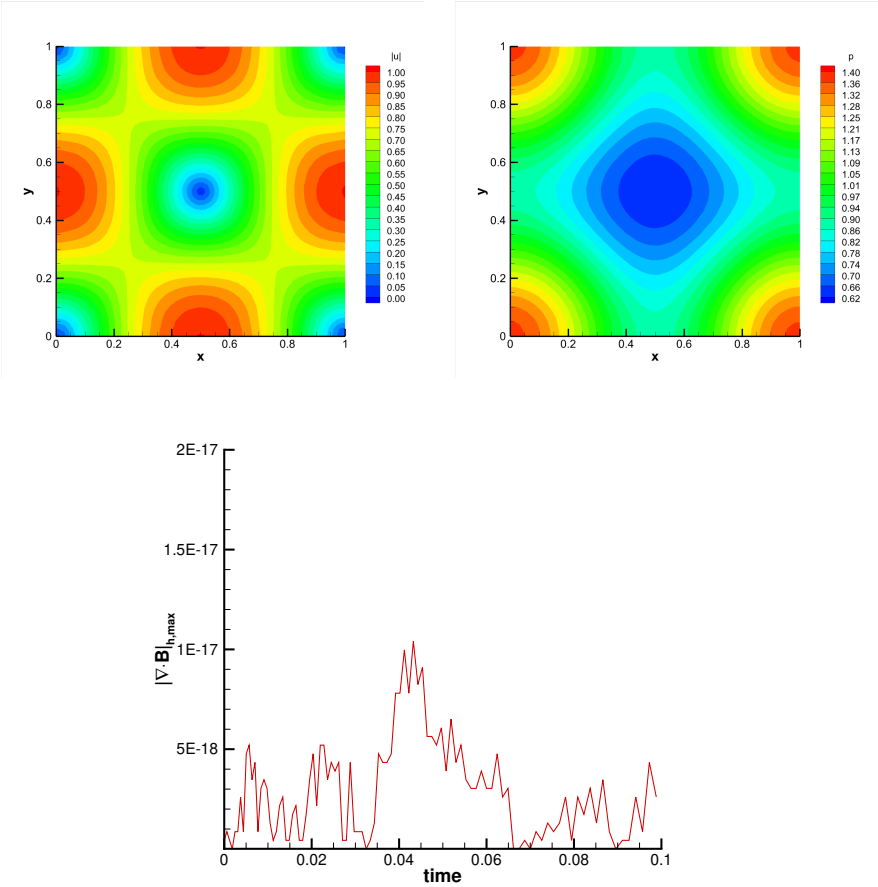

Fig. 4 MHD Taylor-Green vortex test for numerical convergence studies. Magnitude of the velocity (top left) and pressure (top right) field and time evolution of the maximum value of $|\nabla \cdot \boldsymbol{B}|_{h,\max}$ (bottom).

test problems, these shock tube problems become fully multidimensional in the unstructured case, where no mesh edges are in principle aligned with the main flow field. Therefore, these Riemann problems also represent a good test to demonstrate the ability of the LAM schemes of maintaining a symmetric solution over the entire computational domain. For this reason we always show a scatter plot of the physical variable, which simultaneously account for the values in the whole computational mesh. The reference solution is computed with a second order MUSCL-type TVD Eulerian scheme on a fixed one-dimensional mesh made of 20000 cells.

The comparison between the numerical solution obtained with the new LAM solver and the reference solution is presented in Figures 5-9. The first Riemann problem (RP1) deals with two magnetoacoustic rarefaction waves, while RP2 also involves shock waves traveling to the right border of the domain.

Table 5 Initialization of shock tube problems. Initial states left (L) and right (R) are reported together with the final time of the simulation t_f.

	ρ	u	v	w	p	B_x	B_y	B_z
RP1 (Test 3b in [50]): $t_f = 0.1$								
L	1.0	-1.0	0.0	0.0	1.0	0.0	1.0	0.0
R	1.0	1.0	0.0	0.0	1.0	0.0	1.0	0.0
RP2 (Test 3a in [50]): $t_f = 0.01$								
L	0.1	50.0	0.0	0.0	0.4	0.0	$-1/\sqrt{4\pi}$	$-2/\sqrt{4\pi}$
R	0.1	0.0	0.0	0.0	0.2	0.0	$1/\sqrt{4\pi}$	$2/\sqrt{4\pi}$
RP3 (Test 1b in [50]): $t_f = 0.03$								
L	1.0	0.0	0.0	0.0	1.0	$3/\sqrt{4\pi}$	$5/\sqrt{4\pi}$	0.0
R	0.1	0.0	0.0	0.0	10.0	$3/\sqrt{4\pi}$	$2/\sqrt{4\pi}$	0.0
RP4 (Test 4a in [50]): $t_f = 0.15$								
L	1.0	0.0	0.0	0.0	1.0	1.0	1.0	0.0
R	0.2	0.0	0.0	0.0	0.1	1.0	0.0	0.0
RP5 (Test 4b in [50]): $t_f = 0.15$								
L	0.4	-0.66991	0.98263	0.0	0.52467	1.3	0.0025293	0.0
R	1.0	0.0	0.0	0.0	1.0	1.3	1.0	0.0
RP6 (Test 4c in [50]): $t_f = 0.15$								
L	0.65	0.667	-0.257	0.0	0.50	0.75	0.55	0.0
R	1.0	0.4	-0.940	0.0	0.75	0.75	0.0	0.0
RP7 (Brio-Wu problem [14]): $t_f = 0.1$								
L	1.0	0.0	0.0	0.0	1.0	0.75	1.0	0.0
R	0.125	0.0	0.0	0.0	0.1	0.75	-1.0	0.0
RP8 (Test 5b in [50]): $t_f = 0.16$								
L	1.0	0.0	0.0	0.0	1.0	1.3	1.0	0.0
R	0.4	0.0	0.0	0.0	0.4	1.3	-1.0	0.0

Figures 5-6 plot the map of the cell order at the final time, highlighting in red the zones which undergo the *a posteriori* limiting strategy. Similarly, the percentage of detected bad cells requiring the limiting procedure is shown. The results are in good agreement with the reference solution and with other schemes in the literature [25]. Table 6 reports a convergence analysis along the lines of [54] for RP1 and RP2, where the errors are computed in the L_1 norm, aiming at demonstrating the convergence behavior of the LAM scheme in shock tube problems. Since discontinuities are present in both solutions, we can expect no more than first order convergence.

Figure 7 collects the results for Riemann problems RP3-RP6 and depict a comparison for density, horizontal velocity and magnetic field component B_y. Overall one can appreciate that the complex wave structure of the ideal MHD equations is captured by our LAM schemes, although some oscillations are visible especially in the density distribution for RP4 and RP6.

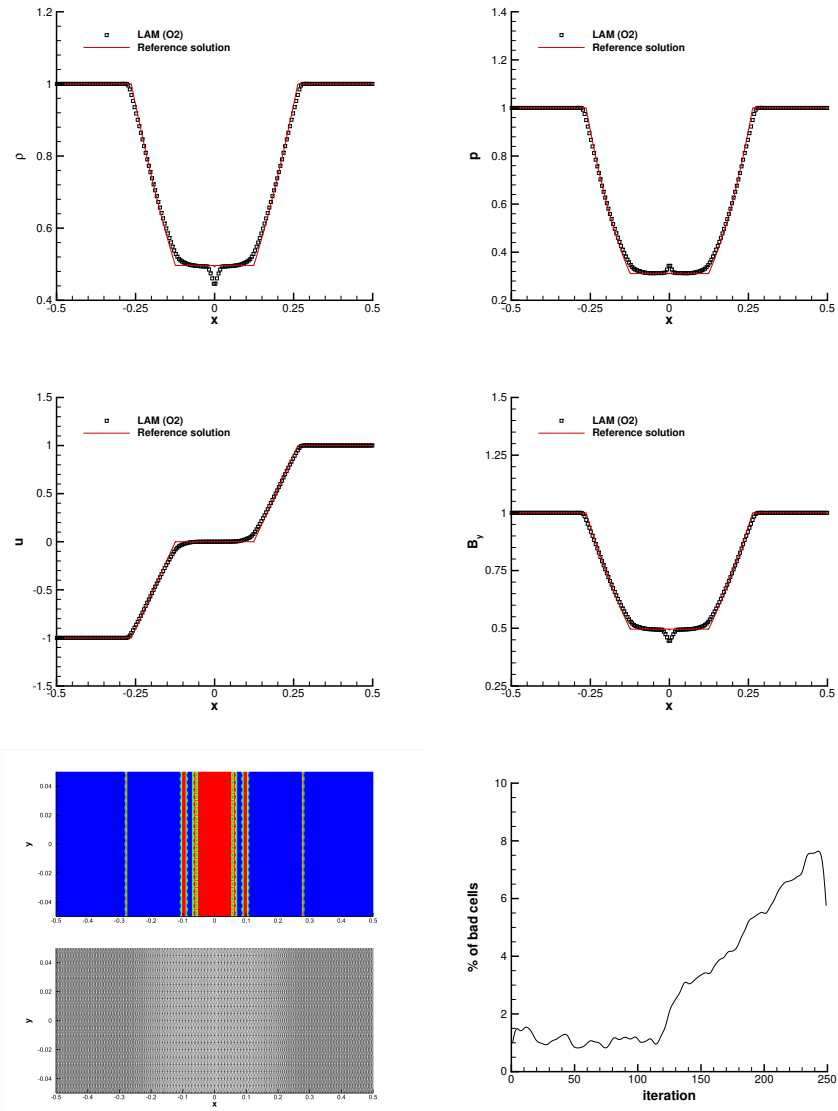

Fig. 5 MHD shock tube problem RP1 at time $t_f = 0.1$. Numerical solution for density, pressure, horizontal velocity, magnetic field component B_y, cell order map with mesh configuration and percentage of detected bad cells at each iteration (from top left to bottom right).

Riemann problem RP7 is the one of Brio and Wu [14] for which a compound wave is produced in the density distribution, as common to all standard finite volume schemes. Notice that, in the Lagrangian framework, the computational domain significantly deforms in $y-$direction, hence making this test

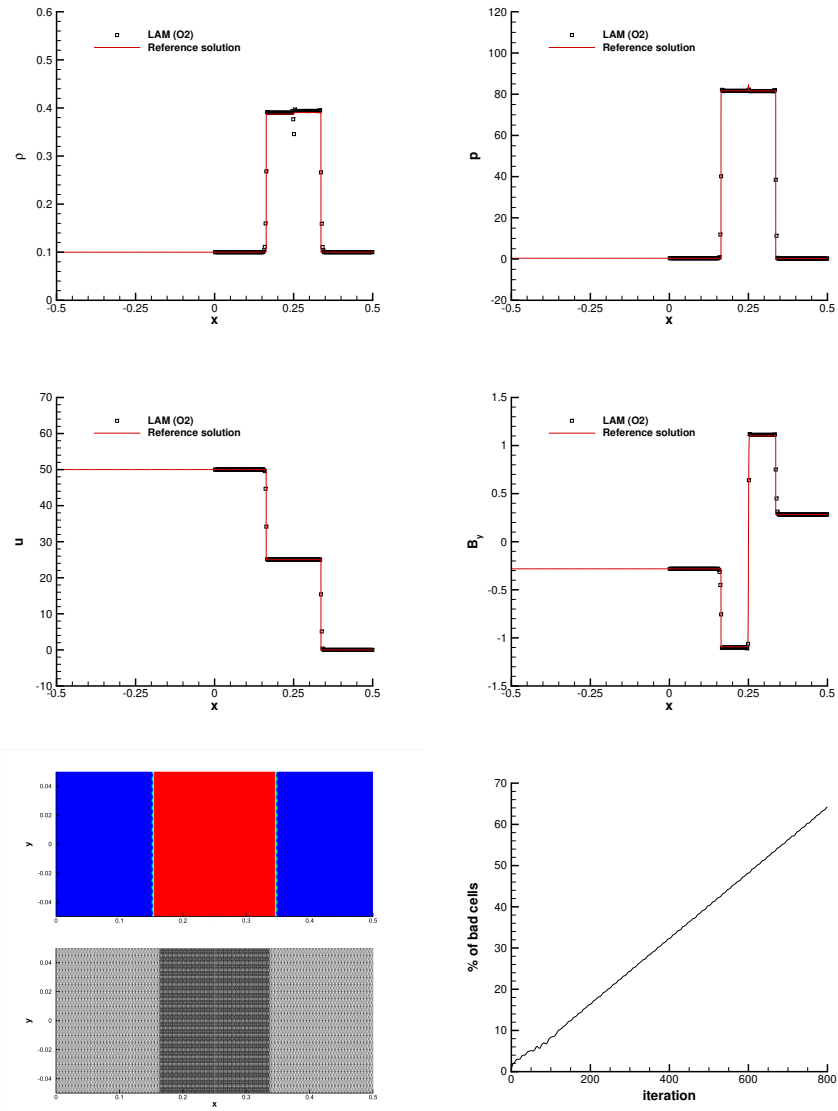

Fig. 6 MHD shock tube problem RP2 at time $t_f = 0.01$. Numerical solution for density, pressure, horizontal velocity, magnetic field component B_y, cell order map with mesh configuration and percentage of detected bad cells at each iteration (from top left to bottom right).

case more difficult compared to the Eulerian framework. Nevertheless, the solution exhibit excellent symmetric properties and the limited cells are correctly identified across the main shock wave.

The last Riemann problem RP8 is run on two different meshes with $h = 1/200$ and $h = 1/400$, and the results are depicted in Figure 9. Our scheme

Table 6 Numerical convergence results for the ideal MHD equations using the *first order* Lagrangian ADER-MOOD (LAM) scheme applied to the MHD shock tube problems RP1 and RP2. The errors are measured in L_1 norm and refer to the variables ρ (density), u (horizontal velocity), p (pressure) and B_y (magnetic field component in y direction) at the final time of each simulation.

MHD shock tube problem RP1

$h(\omega(t_f))$	$L_1(\rho)$	$\mathcal{O}(\rho)$	$L_1(u)$	$\mathcal{O}(u)$
4.00E-02	4.726E-02	-	1.487E-01	-
2.00E-02	3.453E-02	0.45	9.706E-02	0.62
1.00E-02	2.317E-02	0.58	6.023E-02	0.69
5.00E-03	1.473E-02	0.65	3.627E-02	0.73

$h(\omega(t_f))$	$L_1(p)$	$\mathcal{O}(p)$	$L_1(B_y)$	$\mathcal{O}(B_y)$
4.00E-02	9.265E-02	-	4.726E-02	-
2.00E-02	5.774E-02	0.68	3.453E-02	0.45
1.00E-02	3.593E-02	0.68	2.317E-02	0.58
5.00E-03	2.161E-02	0.73	1.473E-02	0.65

MHD shock tube problem RP2

$h(\omega(t_f))$	$L_1(\rho)$	$\mathcal{O}(\rho)$	$L_1(u)$	$\mathcal{O}(u)$
4.00E-02	9.905E-02	-	4.949E-02	-
2.00E-02	3.881E-02	1.35	1.602E-02	1.63
1.00E-02	2.504E-02	0.63	9.423E-03	0.77
5.00E-03	1.610E-02	0.64	6.005E-03	0.65

$h(\omega(t_f))$	$L_1(p)$	$\mathcal{O}(p)$	$L_1(B_y)$	$\mathcal{O}(B_y)$
4.00E-02	1.426E-01	-	1.637E-01	-
2.00E-02	4.976E-02	1.52	4.634E-02	1.82
1.00E-02	3.034E-02	0.71	3.030E-02	0.61
5.00E-03	1.957E-02	0.63	1.698E-02	0.84

presents some difficulties in capturing the second and third waves from the left, which is particularly evident looking at the solution for B_y. We infer that this might be due to our 3-wave approximate Riemann solver.

Finally, Figure 10 shows a three-dimensional view of the density distribution for RP1-RP2 together with a mesh convergence analysis for the same Riemann problems. The errors related to the discretization of the magnetic field divergence are also reported, demonstrating that the involution $\nabla \cdot \boldsymbol{B}$ is preserved up to machine precision for all shock tube tests shown in this section.

6.4 Super-fast expansion

This numerical experiment [20, 55] is characterized by two rarefaction waves moving in opposite direction with each other and pointing towards the left and right border of a one-dimensional domain initially given by $\omega(0) = [-0.5;\ 0.5] \times [-0.05;\ 0.05]$. Periodic boundaries are imposed in $y-$direction while pressure boundary conditions are set in $x-$direction. The fluid undergoes a super-fast expansion which generates a region of very low density and

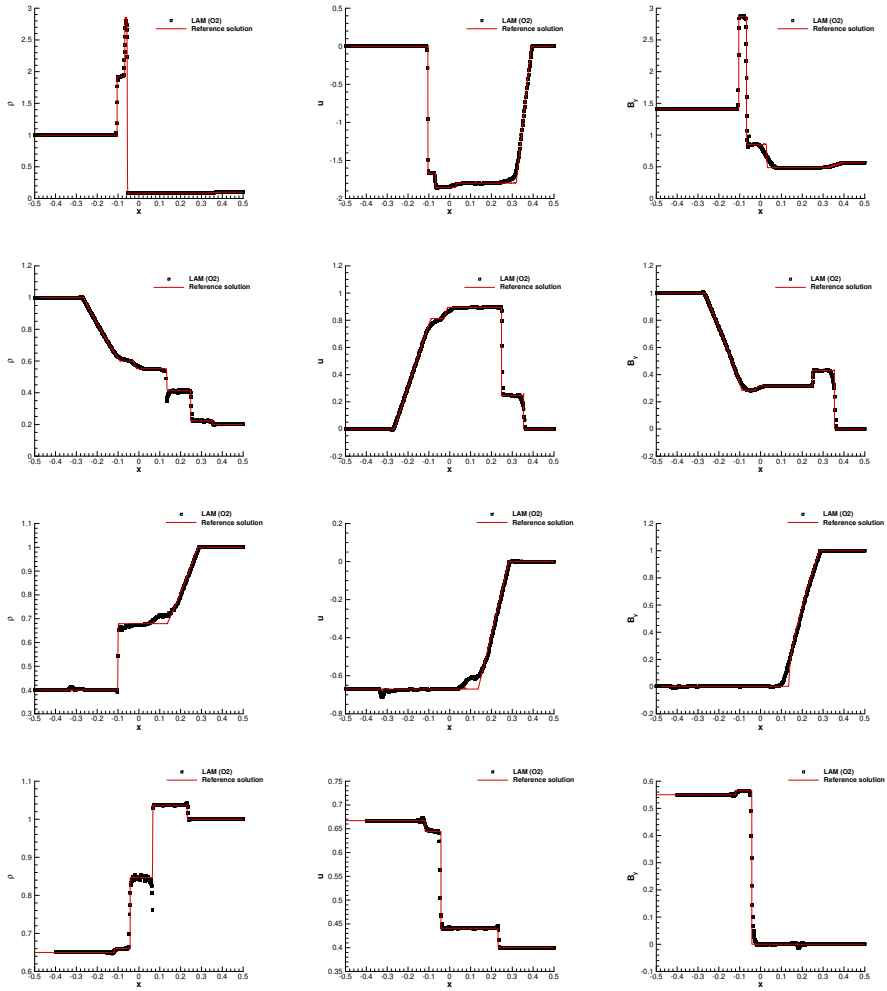

Fig. 7 MHD shock tube problems RP3-RP6. Numerical solution for density (left), horizontal velocity (middle) and magnetic field component B_y (right) for RP3, RP4, RP5, RP6 (from top to bottom row).

pressure along the center of the domain. Therefore, the ability of the numerical scheme of preserving positivity of density and pressure plays a crucial role in this test, which fails for linearized Riemann solvers [55]. The initial condition is given by

$$\mathbf{V}(\boldsymbol{x},0) = \begin{cases} (1,-3.1,0,0,10^{-12},0.5,0,1) & x \leq 0 \\ (1,-3.1,0,0,10^{-12},0.5,0,1) & \text{otherwise} \end{cases}, \tag{77}$$

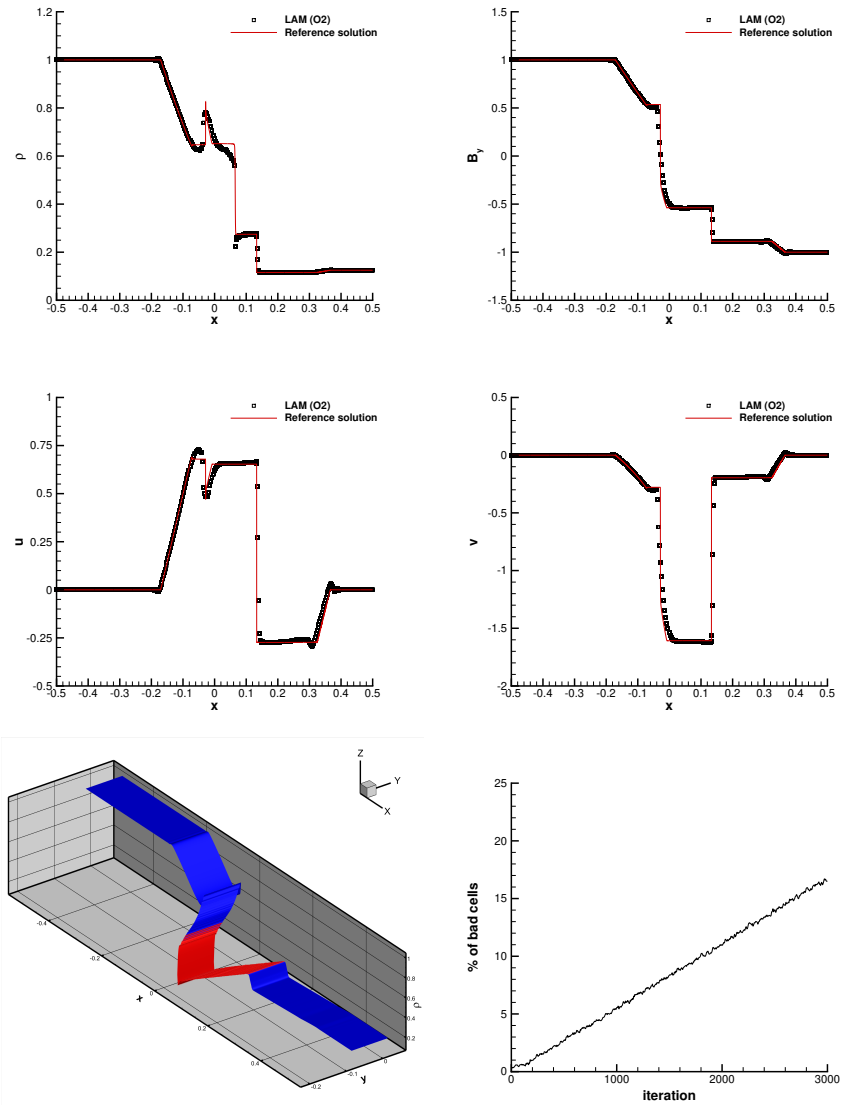

Fig. 8 MHD shock tube problem RP7 at time $t_f = 0.1$. Numerical solution for density, magnetic field component B_y, velocity component u, velocity component v, three-dimensional view of density distribution with cell order map and percentage of detected bad cells at each iteration (from top to bottom).

and the ratio of specific heats is $\gamma = 5/3$. The final time is set to $t_f = 0.1$ and the test problem is run on a sequence of three refined meshes, with characteristic mesh size $h = 1/\eta$, $\eta = \{100, 200, 400\}$. Figure 11 shows mesh convergence results for density and pressure distribution, along with the time evolution of the maximum magnitude of the magnetic field divergence (which remains at

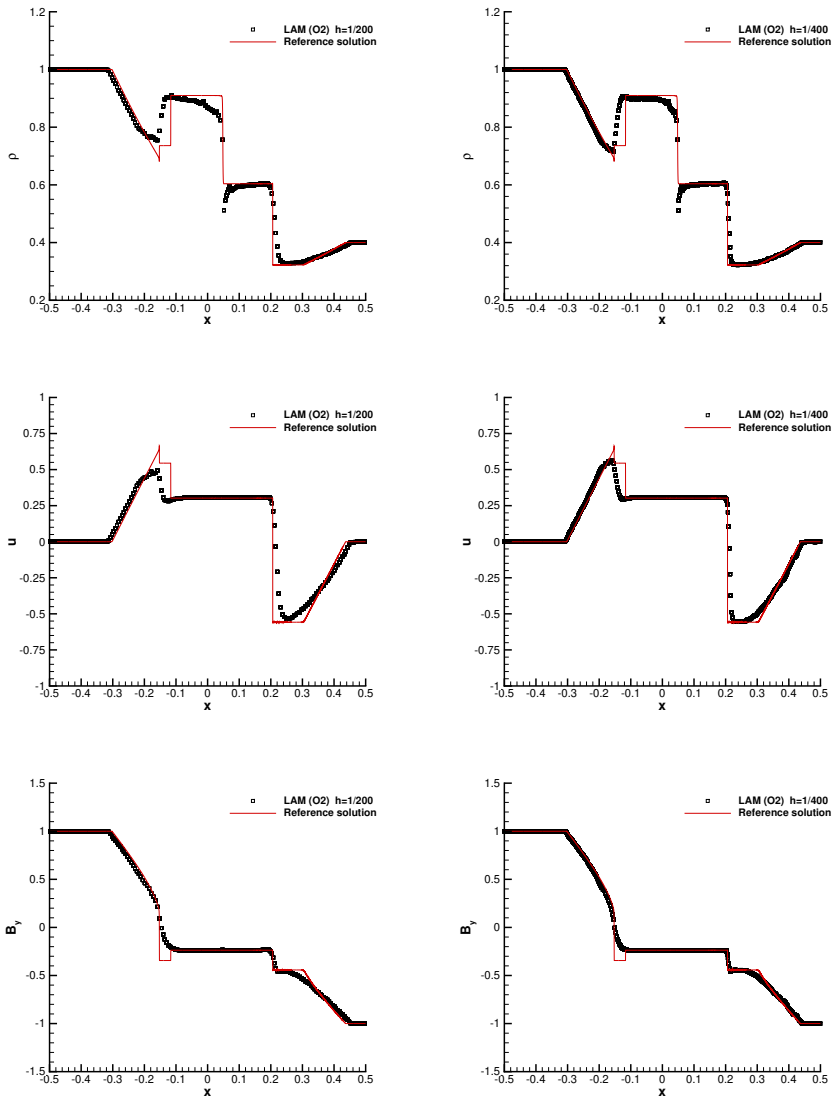

Fig. 9 MHD shock tube problem RP8 at time $t_f = 0.16$. Numerical solution for density (top), horizontal velocity (middle) and magnetic field component B_y (bottom) with characteristic mesh size $h = 1/200$ (left column) and $h = 1/400$ (right column row).

machine precision) and the cell order map with the mesh configuration at the final time. Due to the strong expansion, the control volumes at the center of the domain are highly stretched, and the MOOD limiter acts mostly in this region in order to retrieve positivity of density and pressure, according to the prescribed detection criteria.

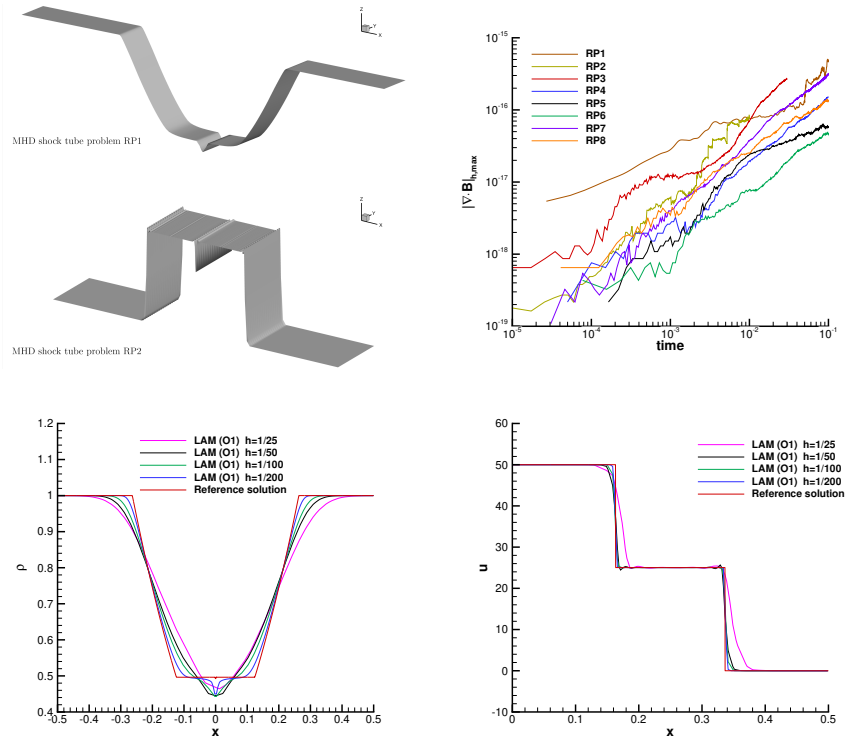

Fig. 10 MHD shock tube problems. Top: three-dimensional view of the density distribution for RP1-RP2 (left) and time evolution of the maximum value of $|\nabla\cdot\boldsymbol{B}|_{h,\max}$ for all shock tube problems RP1-RP8 (right). Bottom: mesh convergence of the first order solution towards the reference solution for density in RP1 (left) and horizontal velocity in RP2 (right).

6.5 3D shear waves test problem

This test problem is taken from [21] and it is characterized by a stationary Alfvén wave in a periodic domain $\omega(0) = [-0.5;\ 0.5] \times [-0.05;\ 0.05]^2$. The gas with ratio of specific heats $\gamma = 5/3$ is initially assigned the following condition:

$$\mathbf{V}(\boldsymbol{x}, 0) = (1, 1, \sin(2\pi x), \cos(2\pi x), p_0, 1, \sin(2\pi x), \cos(2\pi x)), \tag{78}$$

where the uniform pressure is given two values, namely $p_0 = 1$ and $p_0 = 100$, as done in [21]. Differently from the algorithm designed in [21], where this test was run on a one-dimensional Cartesian grid, here we adopt a fully 3D unstructured composed of tetrahedra with characteristic mesh size $h = 1/100$ and $h = 1/200$. The final time is $t_f = 0.1$ and the results are plot in Figure 12 for the second order LAM scheme. The Lagrangian setting is furthermore responsible for a deformation of the computational domain, which does not take place in the Eulerian framework on fixed grids. The profile of the magnetic field component B_y is in very good agreement with the 3-wave

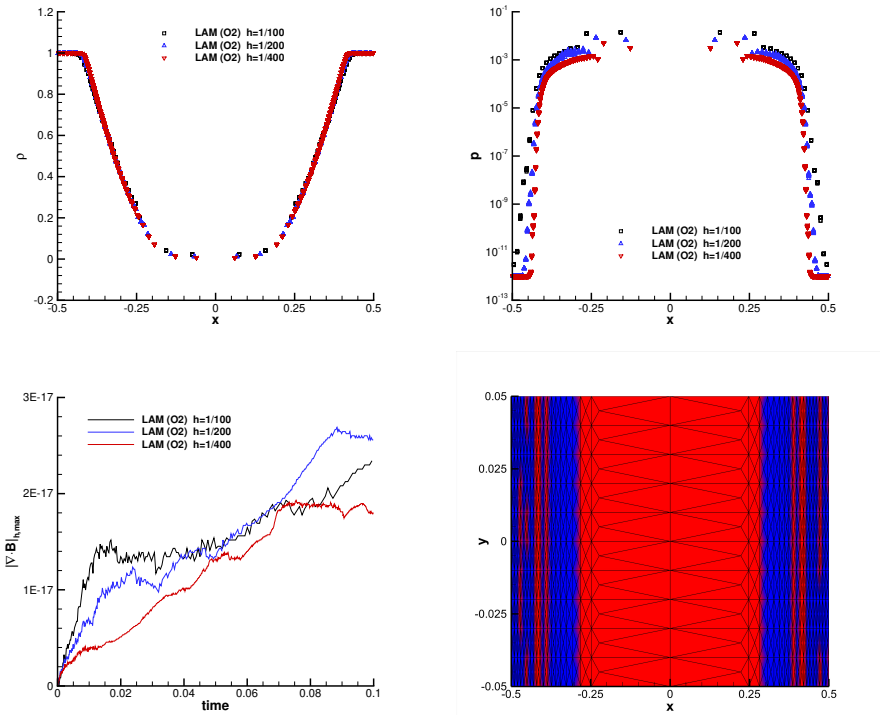

Fig. 11 MHD super-fast expansion test. Top: mesh convergence for second order solution for density (left) and pressure (right). Bottom: time evolution of the maximum value of $|\nabla \cdot \boldsymbol{B}|_{h,\max}$ (left) and cell order map with mesh configuration for $h = 1/100$ (right).

solver proposed in [21]. We show a scatter plot of the numerical solution, that highlights the capability of the novel LAM scheme of maintaining the one-dimensional symmetry of the physical solution. The involution related to the magnetic field is respected up to precision $\approx 10^{-20}$ for the mesh $h = 1/200$, which is mainly due by the remarkable reduction of detected bad cells, as evident from the top panels of Figure 12. In all the four settings of this test case the maximum value of the divergence of the magnetic field never exceeded the threshold 10^{-7}. Table 7 reports the convergence rate of the variables B_y and w measured in L_∞ norm between two consecutively meshes with $h = 1/100$ and $h = 1/200$.

6.6 2D MHD rotor problem

The MHD rotor problem [11] is a benchmark for testing numerical methods for the ideal MHD equations. The initial computational domain is the unit square $\omega(0) = [-0.5;\ 0.5]^2$ which is split into an *internal* and an *external* region by the internal frontier located at radius $R = 0.1$, where $r = \sqrt{\boldsymbol{x} \cdot \boldsymbol{x}}$ denotes the generic radial position. Pressure boundary conditions are prescribed on

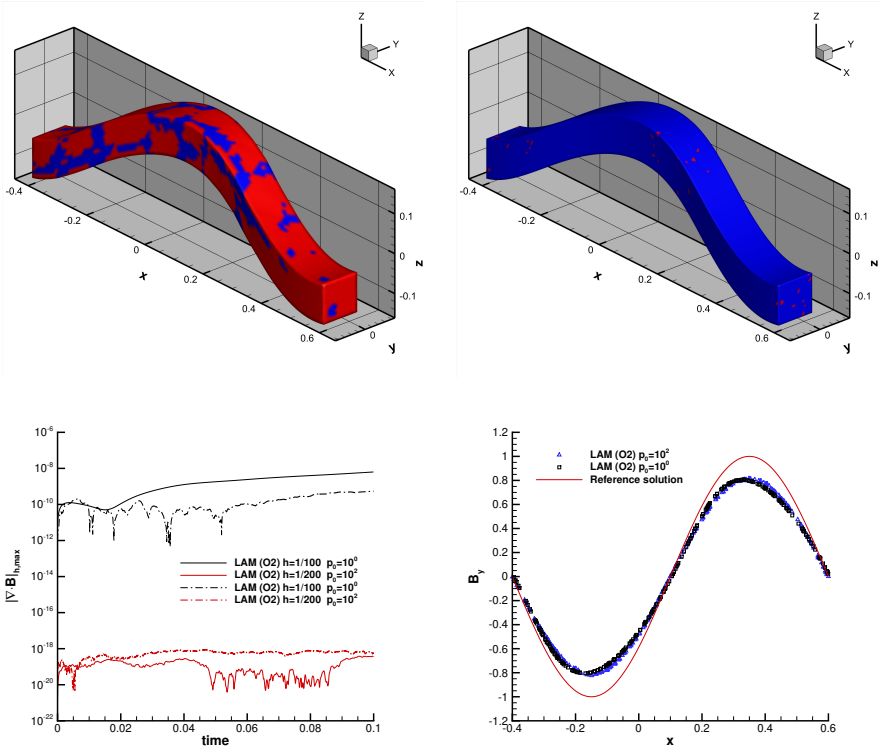

Fig. 12 MHD shear wave problem. Top: three-dimensional computational domain with cell order map for $h = 1/100$ (left) and $h = 1/200$ (right) with $p_0 = 1$. Bottom: time evolution of the maximum value of $|\nabla \cdot \boldsymbol{B}|_{h,\max}$ (left) and comparison of the magnetic field component B_y against the reference solution (right) for both simulations with $p_0 = 1$ and $p_0 = 100$.

Table 7 Numerical convergence rates of the Lagrangian ADER-MOOD (LAM) scheme applied to the MHD shear wave problem with $p_0 = 1$. The errors are measured in L_∞ norm and refer to the variable B_y (magnetic field component in y direction) and w (vertical velocity) at the final time $t_f = 0.1$.

h	$L_\infty(B_y)$	$\mathcal{O}(B_y)$	$L_\infty(w)$	$\mathcal{O}(w)$
1.00E-02	4.8149E-03	-	5.7156E-02	-
5.00E-03	5.6400E-04	3.09	2.1154E-02	1.48

all sides of the domain. A rotating high density fluid (the rotor) is embedded in a low density atmosphere at rest. The pressure is initially uniformly set to $p = 1$, while the initial density distribution is $\rho = 10$ for $0 \leq r \leq R$ and $\rho = 1$ elsewhere. The velocity field is zero in the external region, whereas inside the rotor it is given by $\boldsymbol{v} = \boldsymbol{\theta} \times \boldsymbol{x}$ with $\boldsymbol{\theta} = (0, 0, 10)$. As the simulation goes on, the angular momentum of the rotor is diminishing, because of the Alfvén waves produced by the rotor. The ratio of specific heats is taken to be $\gamma = 1.4$ with $\mu_0 = 4\pi$, and the simulation is run until the final time $t_f = 0.25$. We use an unstructured computational grid with a characteristic mesh size of $h = 1/200$,

yielding a total number of $N_E = 71046$ control volumes. The Courant number is set to $C_{\text{CFL}} = 1$ for this test. The numerical results are plot in Figure 13, achieving a good agreement with the solution presented in [11], despite the coarser mesh resolution. We use 41 contour levels in the range [1; 10] for the density, [0.1; 1.25] for the pressure, [0.05; 0.8] for the magnetic pressure, [0; 1.55] for the Mach number. The limited cells are mainly located along the discontinuities induced by the rotor and the divergence-free involution is again preserved up to machine precision.

6.7 MHD Orszag-Tang vortex system

Another well-established test problem is the Orszag-Tang vortex system [56], with the setup proposed in [57]. This problem is initialized on a periodic domain spanning $\omega(0) = [0;\ 2\pi]^2$, which is discretized with a triangular mesh composed of $N_E = 69614$ elements with characteristic mesh size of $h = 1/150$. The ratio of specific heats is $\gamma = 5/3$ and we set $\mu_0 = 4\pi$, according to [47, 53]. The fluid is initially assigned a density $\rho = \gamma^2$, a velocity field $\boldsymbol{v} = (-\sin(y), \sin(x), 0)$ and a magnetic field $\boldsymbol{B} = \sqrt{4\pi}(-\sin(y), \sin(2x), 0)$. Complex wave patterns arise during the simulation and the computational domain quickly becomes highly distorted. The final time of the simulation is $t_f = 2$ and the results are plot in Figure 14 at three different output times. Both the pressure distribution and the cell order map are shown, and our results very well match those ones obtained in [53], with the same number of contour lines for the pressure adopted here.

Finally, Figure 15 shows the percentage of detected bad cells at each iteration and the time evolution of the constraint $\nabla \cdot \boldsymbol{B}$, that is correctly preserved throughout the entire computation.

6.8 MHD cloud-shock interaction

We consider a moving shock hitting a cloud at rest with high density. The interaction between the shock and the cloud produces a bow shock in the front along with tail shocks in the rear, thus generating complex turbulent-like structures which highly twist and stretch the cells in the Lagrangian mesh. The setup of this test case follows from [55], where a high order finite volume scheme on fixed grid was used to run the simulation until the final time $t_f = 0.06$. Here, despite the moving mesh approach, we still maintain the same setting hence making this test even more challenging due to the strong mesh deformations that arise from the cloud-shock interaction. The computational domain at the initial time is $\omega(0) = [-0.6;\ 1] \times [0;\ 1]$ with velocity boundary conditions set along the $x-$direction (inflow and outflow borders), whereas zero-velocity (slip-wall condition) is imposed in $y-$direction. The shock front is located at $x = 0.05$ when the simulation starts. The cloud has initially a radius of $R = 0.15$ and it is centered in $\boldsymbol{x}_b = (0.25, 0.5)$, thus the fluid density is initially

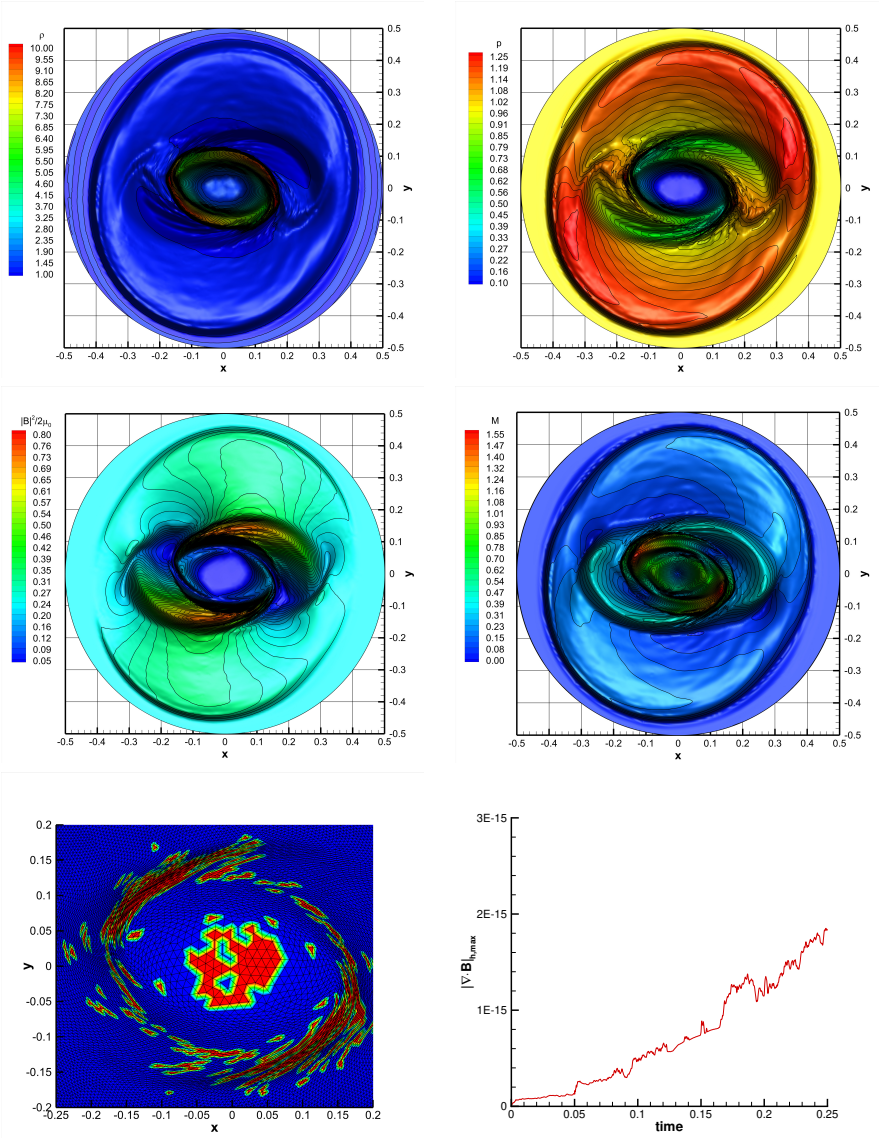

Fig. 13 2D MHD rotor problem at time $t_f = 0.25$. Numerical solution for density, pressure, magnetic pressure, Mach number, cell order map with mesh configuration and time evolution of the maximum value of $|\nabla \cdot \boldsymbol{B}|_{h,\max}$ (from top left to bottom right).

assigned

$$\rho(\boldsymbol{x}, 0) = \begin{cases} 3.86859 & x \leq 0.05 \\ 10 & |\boldsymbol{x} - \boldsymbol{x}_b| \leq R \\ \text{otherwise} & \end{cases} .$$

The other variables are initialized according to a post-shock and a pre-shock state, that are given by

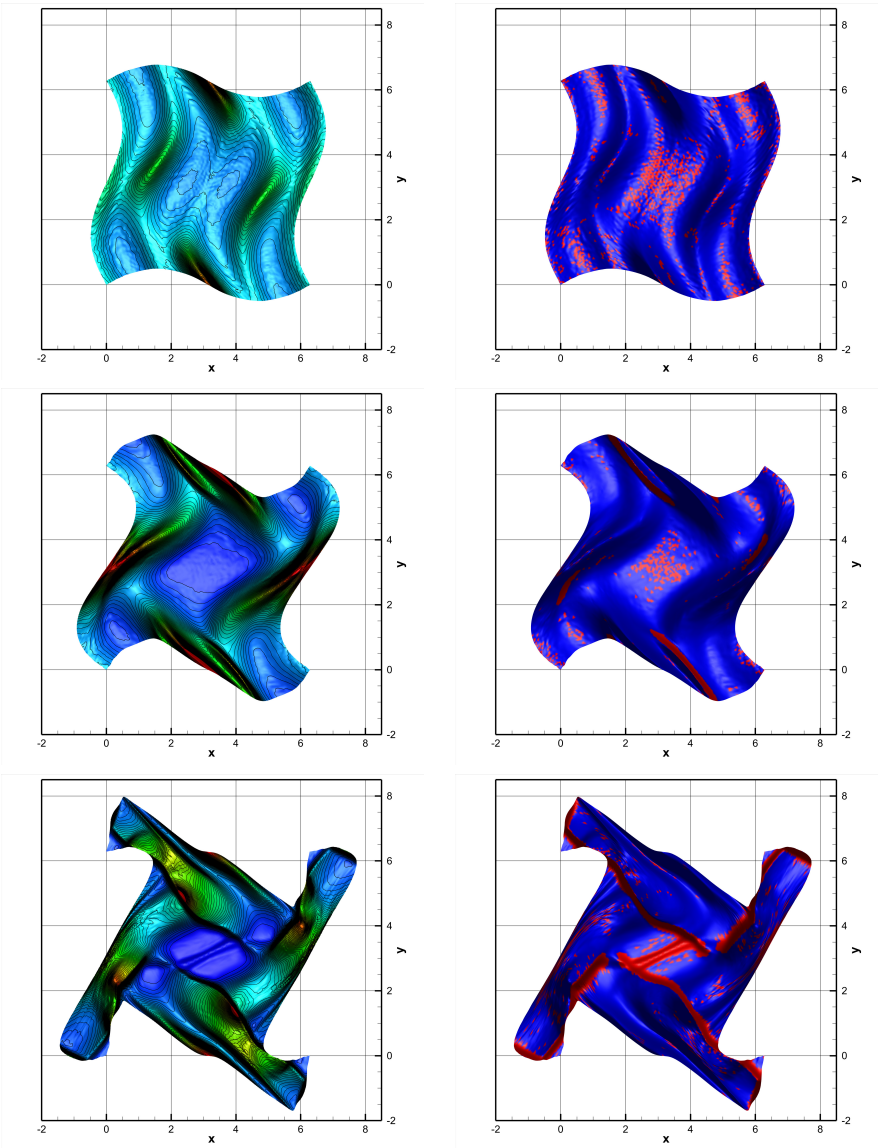

Fig. 14 MHD Orszag-Tang vortex system. Numerical solution for pressure (left) and cell order map (right) obtained at time $t = 0.5$, $t = 1.5$ and $t = 2$ (from top left to bottom right). 56 equidistant contour lines of the pressure are shown in the interval [0.5, 6] are shown.

- For $x \leq 0.05$

$$(u, v, w, p, B_x, B_y, B_z)_1 = (11.2536, 0, 0, 167.345, 0, 2.18261820, -2.18261820).$$

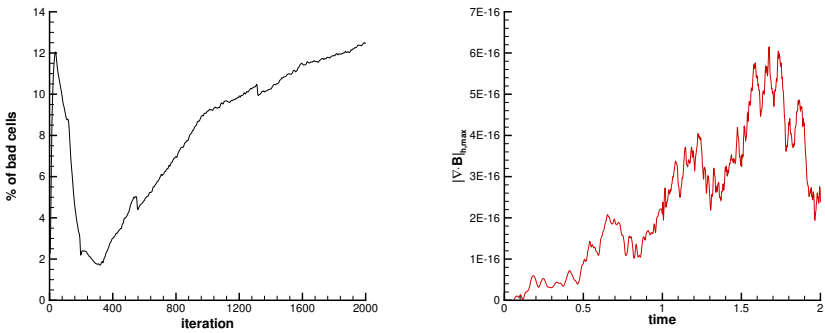

Fig. 15 MHD Orszag-Tang vortex system. Percentage of detected bad cells at each iteration (left) and time evolution of the maximum value of $|\nabla \cdot \boldsymbol{B}|_{h,\max}$.

- For $x > 0.05$

$$(u, v, w, p, B_x, B_y, B_z)_0 = (1, 0, 0, 1, 0, 0.56418958, 0.56418958).$$

The computational mesh is composed of approximately 250000 unstructured control volumes of characteristic mesh size $h = 1/500$. Figure 16 depicts the second order results for density at time $t = 0.03$ and $t = 0.06$, showing the main shock fronts which are generated from the cloud-shock interaction. The limiting procedure take place mostly across the discontinuities which are very well identified by the MOOD detection criteria. A zoom of the computational mesh close to the gas cloud is also shown, in order to demonstrate the high deformations encountered by the control volumes during the simulation. Although the grid is not symmetric and the quality of the mesh rapidly decreases because of the complex flow patterns induced by this test, the numerical solution maintains a very good symmetry until the final time of the simulation, that corresponds to the one used in an Eulerian framework on fixed meshes [55].

The simulation is run also on two coarser meshes, namely with mesh size $h = 1/125$ and $h = 1/250$. Figure 17 plots the total energy distribution and the magnetic pressure at the final time for all three mesh configurations. The range of the energy spans the interval $[0;\ 2200]$ and it is in accordance with the numerical results presented in [55], and mesh convergence can be qualitatively appreciated.

6.9 MHD blast wave problem in 2D and 3D

The last test case is the MHD blast wave problem firstly originally presented in [47], which is a notoriously difficult test case. As the plasma's β becomes smaller, this problem becomes increasingly stringent. The quantity β measures the ratio of the thermal pressure to the magnetic pressure.

The 2D setup is taken from [25], thus the initial condition of the fluid is $\mathbf{V}(\boldsymbol{x}, 0) = (1, 0, 0, 0, p(r), 5\sqrt{2}, 5\sqrt{2}, 0)$ with the pressure distribution given as

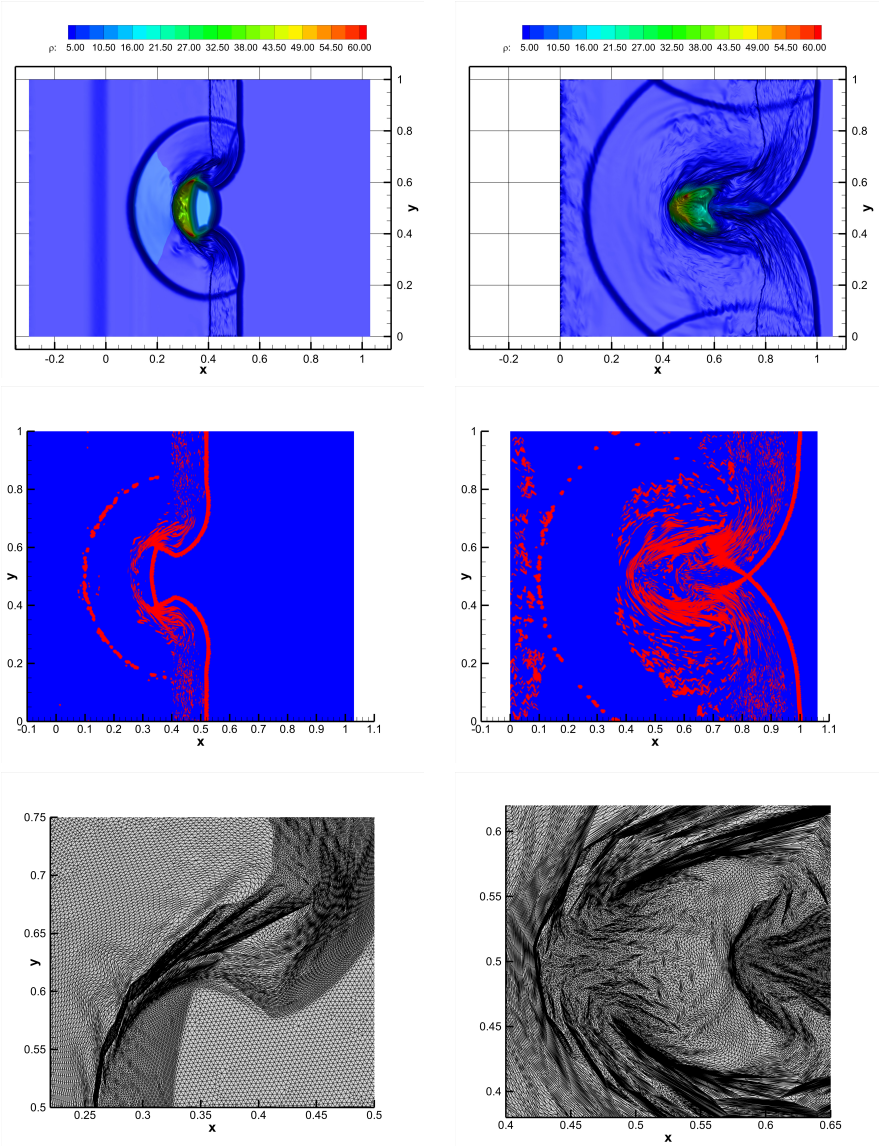

Fig. 16 MHD cloud-shock interaction problem at time $t = 0.03$ (left column) and $t = 0.06$ (right column). Top: second order numerical solution for density. Middle: cell order map. Bottom: zoom of the mesh configuration close to the gas cloud.

a function of the radial position $r = \sqrt{\boldsymbol{x} \cdot \boldsymbol{x}}$:

$$p(r) = \begin{cases} 1 & r \leq 0.125 \\ 100 & \text{otherwise} \end{cases}, \qquad \text{in 2D.} \tag{79}$$

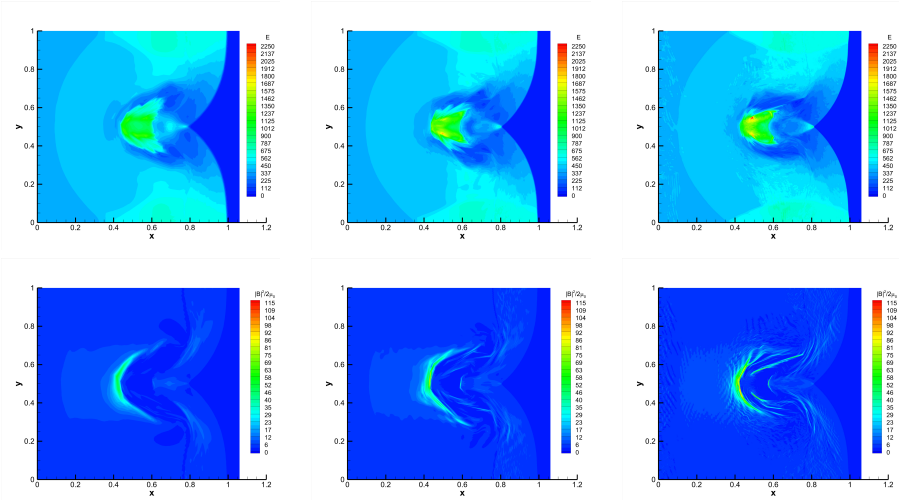

Fig. 17 MHD cloud-shock interaction problem at time $t = 0.06$. Energy distribution in the interval $[0;\ 2200]$ (top row) and magnetic pressure in the interval $[0.1;\ 115]$ (bottom row) for mesh size $h = 1/125$ (left), $h = 1/250$ (middle) and $h = 1/500$ (right).

The computational domain is the square $\omega(0) = [-0.5;\ 0.5]^2$ with pressure boundaries imposed everywhere. An unstructured grid of characteristic size $h = 1/100$ with $N_E = 22882$ triangles is used to pave the domain. The numerical results are shown in Figure 18 at the final time $t_f = 0.02$, which are in excellent agreement with the literature [58]. We use 41 contour levels in the range $[0.25;\ 3.8]$ for the density, $[0.5;\ 35]$ for the pressure, $[25;\ 75]$ for the magnetic pressure. The mesh is highly compressed by the shock wave and the magnetic field involution is preserved up to machine precision.

For the three-dimensional setup we use $\mu_0 = 4\pi$ and the pressure field is initially assigned according to [59] as

$$p(r) = \begin{cases} 0.1 & r \leq 0.1 \\ 1000 & \text{otherwise} \end{cases}, \qquad \text{in 3D}, \tag{80}$$

hence allowing for a pressure jump of four orders of magnitude. The initial data for the remaining flow variables are given by $\mathbf{V}(\boldsymbol{x}, 0) = (1, 0, 0, 0, p(r), 50/\sqrt{3}, 50/\sqrt{3}, 50/\sqrt{3})$. The value of the plasma's β is initially given by $\beta = 1.005 \cdot 10^{-3}$. The computational domain is the sphere of radius $R = 0.5$, that is discretized with a tetrahedral mesh of characteristic size $h = 0.015$, hence leading to a total number of $N_E = 1'090'261$ control volumes. The final time of the simulation is $t_f = 0.012$ and the numerical results are reported in Figure 19, along a slice on the xy plane extracted at $z = 0$. The numerical solution is qualitatively in good agreement with the results presented in [59]. We show the logarithm of density and pressure (41 contour levels in the range $[-0.85;\ 0.25]$ and $[-1;\ 1.9]$, respectively) as well as the magnitude of both the velocity and the magnetic field (41 contour levels in the range $[0;\ 7.5]$

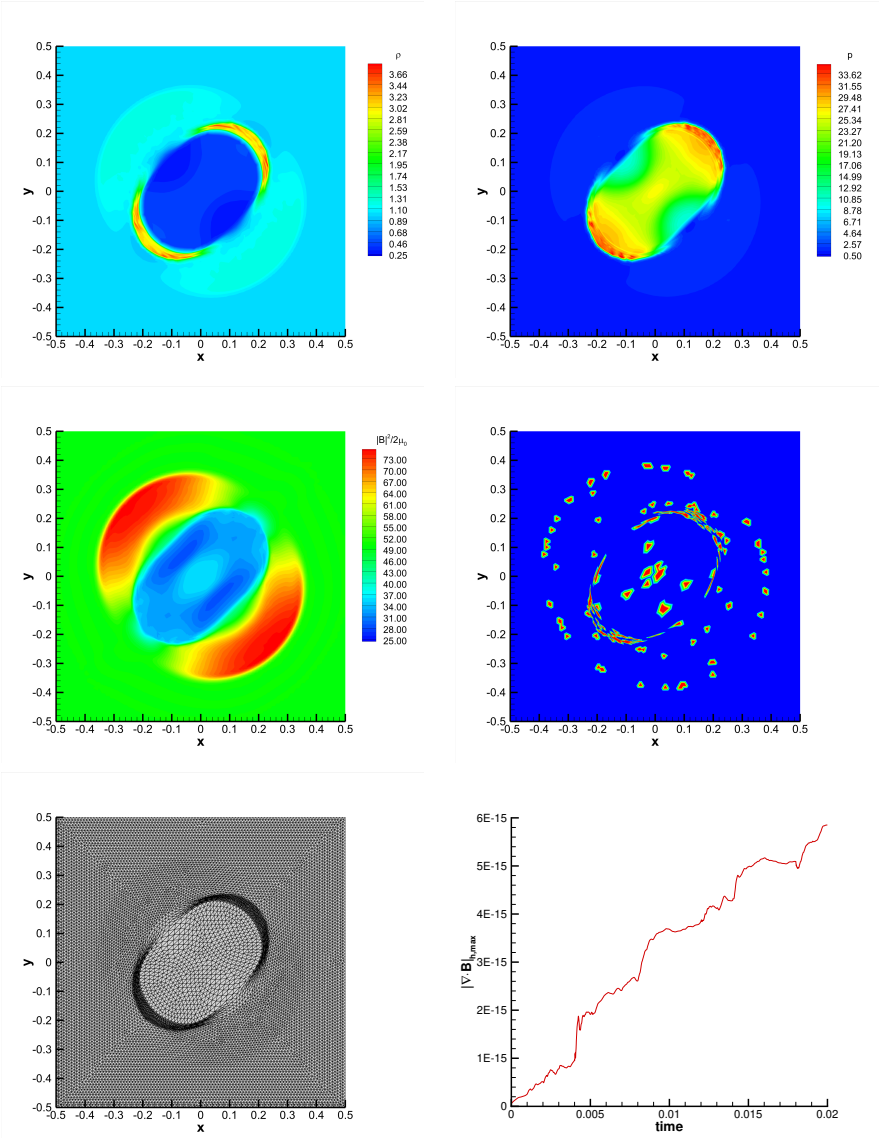

Fig. 18 2D MHD blast wave problem at time $t_f = 0.02$. Numerical solution for density, pressure, magnetic pressure, cell order map, mesh configuration and time evolution of the maximum value of $|\nabla \cdot \boldsymbol{B}|_{h,\max}$ (from top left to bottom right).

and [15; 63], respectively). The number of detected bad cells is quite low and those cells are mostly located at the shock front, as expected. Figure 20 plots the time evolution of the error related to the divergence-free involution, which is very well preserved even in the 3D case on unstructured meshes.

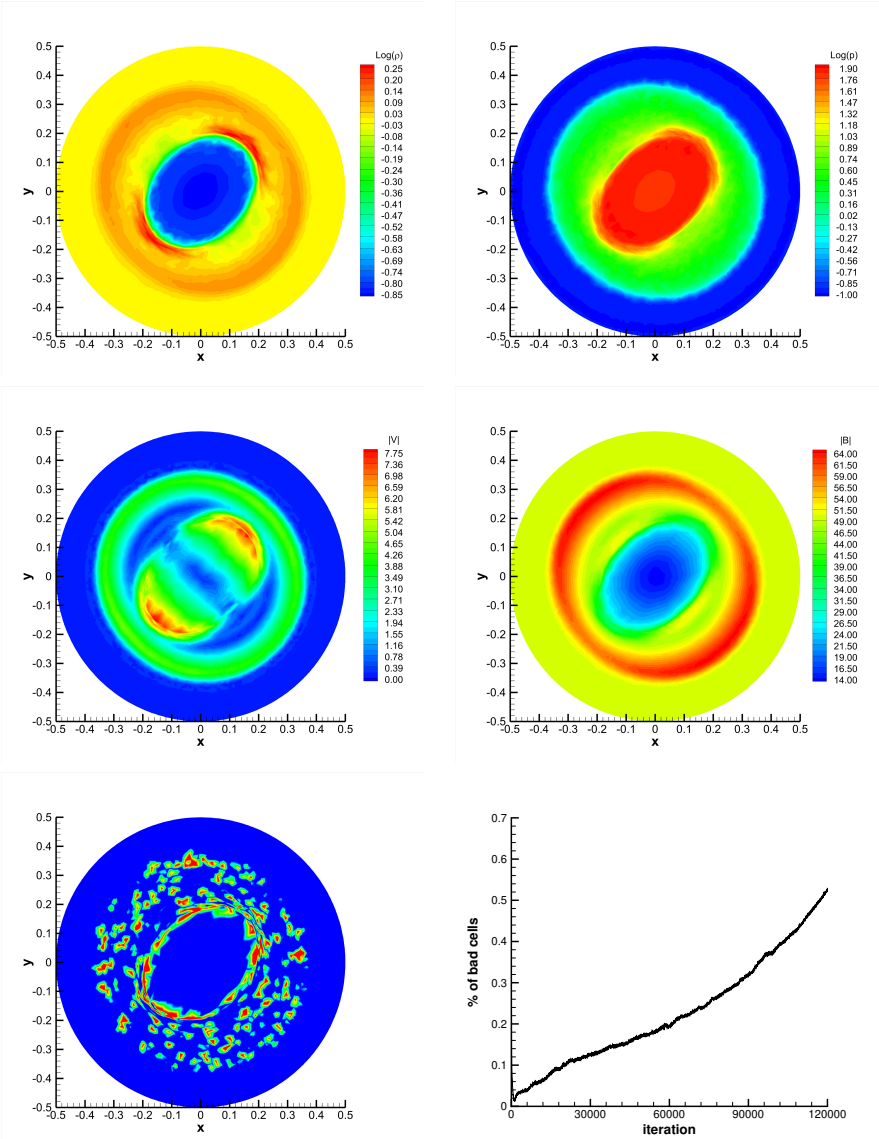

Fig. 19 3D MHD blast wave problem at time $t_f = 0.012$ along the slice $z = 0$. Numerical solution for logarithmic density, logarithmic pressure, magnitude of the velocity and the magnetic field, cell order map and percentage of detected bad cells at each iteration (from top left to bottom right).

7 Conclusion

We have described an unconventional moving mesh Finite Volume discretization for solving Lagrangian ideal MHD over 3D simplicial grid which stems directly from the FV method that we have designed for Lagrangian

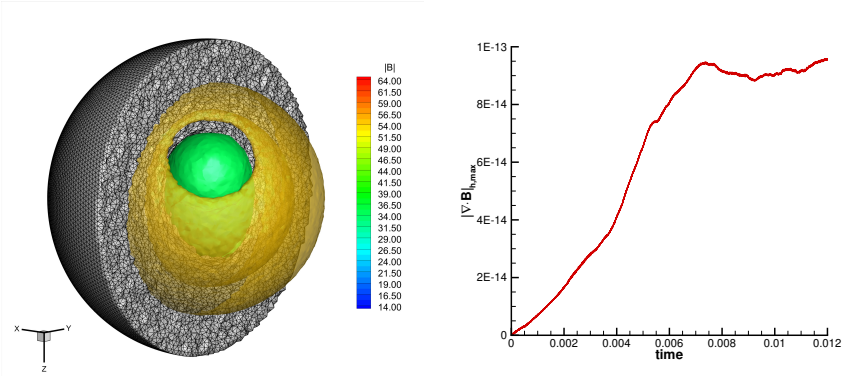

Fig. 20 3D MHD blast wave problem at time $t_f = 0.012$. Sketch of the unstructured tetrahedral mesh together with the iso-contour surfaces of the magnetic field intensity at $|\boldsymbol{B}| = \{35, 55\}$ (left) and time evolution of the maximum value of $|\nabla \cdot \boldsymbol{B}|_{h,\max}$ (right).

hyperelasticity in our previous work [30]. The link between the time evolution of the magnetic field and the deformation gradient which characterizes the Lagrange-to-Euler transformation, provides an elegant approach to cope with the subtle question of the involution that should satisfy the magnetic field. The divergence preservation of the magnetic field is naturally inbuilt in the numerical method since the cell-centered magnetic field is updated in terms of the deformation gradient tensor which is computed through a fully compatible discretization of the Geometrical Conservation Law. The nodal velocity and the sub-face forces approximating the numerical fluxes are computed through a nodal solver while ensuring a semi-discrete entropy inequality and the conservation of momentum and total energy. We have displayed the accuracy and the robustness of our unconventional numerical methods against various representative test cases. It is remarkable that the discrete divergence of the magnetic field computed over the dual cells remains preserved up to the machine precision.

In future works we plan to investigate the extension of this numerical method to general polyhedral grids. We also aim at studying the positivity preserving and the entropy stability of this numerical method at the discrete level in order to provide explicit conditions on the time step to ensure the positivity of specific volume, internal energy and entropy stability. Another direction of research would be to exhibit the structure of the approximate Riemann solvers underlying to the nodal solver.

Acknowledgments

WB received financial support by Fondazione Cariplo and Fondazione CDP (Italy) under the project No. 2022-1895. This work has been undertaken under the auspice of the LRC ANABASE which is a joined research laboratory between Institut de Mathématiques de Bordeaux and CEA-CESTA devoted to

the development of innovative numerical methods for the simulation of complex fluid flows.

Declarations

Competing interests

The authors have no competing interests to declare that are relevant to the content of this article.

Financial interests

The authors have no relevant financial or non-financial interests to disclose.

Ethics approval

On behalf of all authors, the corresponding author is available to collect documentation of compliance with ethical standards and send upon request.

References

[1] Ogilvie, G.I.: LECTURE NOTES Astrophysical fluid dynamics. J. Plasma Phys. **82** (2016)

[2] Derigs, D.: Ideal GLM-MHD - a new mathematical model for simulating astrophysical plasmas. PhD thesis, Universität zu Köln (2018)

[3] Kulikovskii, A.G., Pogorelov, N.V., Semenov, A.Y.: Mathematical Aspects of Numerical Solution of Hyperbolic Systems. Chapman & Hall/CRC, Cambridge, England (1999)

[4] Trangenstein, J.A.: Numerical Solution of Hyperbolic Partial Differential Equations. Cambridge University Press, Cambridge, England (2009)

[5] Powell, K.G.: An approximate Riemann solver for Magnetohydrodynamics (That Works in More than One Dimension). ICASE-Report 94-24, NASA Langley Research Center (1994)

[6] Godunov, S.K.: The symmetric form of magnetohydrodynamics equation. Numerical Methods for Mechanics of Continuum Medium **1**, 26–34 (1972)

[7] Barth, T.: On the Role of Involutions in the Discontinuous Galerkin Discretization of Maxwell and Magnetohydrodynamic Systems. In: Arnold, D.N., Bochev, P.B., Lehoucq, R.B., Nicolaides, R.A., M. Shashkov, M. (eds.) Compatible Spatial Discretizations, pp. 69–88. Springer, New York, NY (2006)

[8] Brackbill, J.U., Barnes, D.C.: The effects of Nonzero $\nabla \cdot \boldsymbol{B}$ on the numerical solution of the magnetohydrodynamics equations. Journal of Computational Physics **35**, 426–430 (1980)

[9] Powell, K.G., Roe, P.L., Linde, T.J., Gombosi, T.I., Zeeuw, D.L.D.: A Solution-Adaptive Upwind Scheme for Ideal Magnetohydrodynamics. Journal of Computational Physics **154**(2), 284–309 (1999)

[10] Evans, C.R., Hawley, J.F.: Simulation of Magnetohydrodynamic Flows: A Constrained Transport Model. Astrophysical Journal **332** (1988)

[11] Balsara, D., Spicer, D.: A staggered mesh algorithm using high order godunov fluxes to ensure solenoidal magnetic fields in magnetohydrodynamic simulations. Journal of Computational Physics **149**, 270–292 (1999)

[12] Dedner, A., Kemm, F., Kröner, D., Munz, C.D., Schnitzer, T., Wessenberg, M.: Hyperbolic Divergence Cleaning for the MHD Equations. Journal of Computational Physics **175**, 645–673 (2002)

[13] Harten, A., Lax, P.D., van Leer, B.: On upstream Differencing and Godunov-Type schemes for Hyperbolic Conservation Laws. SIAM Review **25**(1), 35–61 (1983)

[14] Brio, M., Wu, C.C.: An upwind differencing scheme for the equations of ideal magnetohydrodynamics. Journal of Computational Physics **75**, 400–422 (1988)

[15] Gallice, G.: Positive and Entropy Stable Godunov-Type Schemes for Gas Dynamics and MHD Equations in Lagrangian or Eulerian Coordinates. Numer. Math. **94**(4), 673–713 (2003)

[16] Li, S.: An HLLC Riemann solver for magneto-hydrodynamics. Journal of Computational Physics, 344–357 (2005)

[17] Balsara, D.S.: Multidimensional HLLE Riemann solver: Application to Euler and magnetohydrodynamic flows. Journal of Computational Physics **229**, 1970–1993 (2010)

[18] Balsara, D.S.: A two-dimensional HLLC Riemann solver for conservation laws: Application to Euler and magnetohydrodynamic flows. Journal of Computational Physics **231**, 7476–7503 (2012)

[19] Balsara, D.S.: Multidimensional Riemann problem with self-similar internal structure. Part I Application to hyperbolic conservation laws on structured meshes. Journal of Computational Physics **277**, 163–200 (2014)

[20] Bouchut, F., Klingenberg, C., Waagan, K.: A multiwave HLL approximate Riemann solver for ideal MHD based on relaxation I: theoretical framework. Numer. Math. **108**, 7–42 (2007)

[21] Bouchut, F., Klingenberg, C., Waagan, K.: A multiwave approximate Riemann solver for ideal MHD based on relaxation II: numerical implementation with 3 and 5 waves. Numer. Math. **115**, 647–679 (2010)

[22] Fuchs, F.G., Murry, A.D.M., Mishra, S., Risebro, N.H., Waagan, K.: Approximate Riemann solvers and Robust High-Order Finite Volume Schemes for Multi-Dimensional Ideal MHD equations. Commun. Comput. Phys. **2**, 324–362 (2011)

[23] Derigs, D., Winters, A.R., Gassner, G.J., Walch, S., Bohm, M.: Ideal GLM-MHD: About the entropy consistent nine-wave magnetic field divergence diminishing ideal magnetohydrodynamics equations. Journal of Computational Physics **364**, 420–467 (2018)

[24] Wu, K., Shu, C.-W.: Provably positive high-order schemes for ideal magnetohydrodynamics: Analysis on general meshes. Numerische Mathematik **142**(4), 995–1047 (2019)

[25] Xu, X., Dai, Z., Gao, Z.: A 3D cell-centered Lagrangian scheme for the ideal Magnetohydrodynamics equations on unstructured meshes. Comput. Methods Appl. Mech. Engrg. **342**, 490–508 (2018)

[26] Georges, G., Breil, J., Maire, P.-H.: A 3D GCL compatible cell-centered Lagrangian scheme for solving gas dynamics equations. Journal of Computational Physics **305**, 921–941 (2016)

[27] Boscheri, W., Dumbser, M., Loubère, R., Maire, P.-H.: A second-order cell-centered Lagrangian ADER-MOOD finite volume scheme on multidimensional unstructured meshes for hydrodynamics. J. Comput. Phys. **358**, 103–129 (2018)

[28] Zou, S., Zhao, X., Yu, X., Dai, Z.: A RKDG method for 2D Lagrangian Ideal Magnetohydrodynamics Equations with Exactly Divergence-Free Magnetic Field. Commun. Comput. Phys. **32**, 547–582 (2022)

[29] Després, B.: A new Lagrangian formulation of ideal magnetohydrodynamics. Journal of Hyperbolic Differential Equations **8**, 21–35 (2011)

[30] Boscheri, W., Loubère, R., Maire, P.-H.: A 3D cell-centered ADER MOOD Finite Volume method for solving updated Lagrangian hyperelasticity on unstructured grids. Journal of Computational Physics **449** (2022)

[31] Loubère, R., Maire, P.-H., Rebourcet, B.: Chapter 13 - staggered and colocated finite volume schemes for Lagrangian hydrodynamics. In: Abgrall, R., Shu, C.-W. (eds.) Handbook of Numerical Methods for Hyperbolic Problems Basic and Fundamental Issues. Handbook of Numerical Analysis, vol. 17, pp. 319–352 (2016)

[32] Godlewski, E., Raviart, P.-A.: Numerical Approximation of Hyperbolic Systems of Conservation Laws. Springer, New York (1996)

[33] Gurtin, M.E., Fried, E., Anand, L.: The Mechanics and Thermodynamics of Continua. Cambridge University Press, Cambridge, England (2010)

[34] F.Vilar, Maire, P.-H., Abgrall, R.: A discontinuous Galerkin discretization for solving the two-dimensional gas dynamics equations written under total Lagrangian formulation on general unstructured grids. Journal of Computational Physics **276**, 188–234 (2014)

[35] Janhunen, P.: A Positive Conservative Method for Magnetohydrodynamics Based on HLL and Roe Methods. Journal of Computational Physics **160**, 649–661 (2000)

[36] Maire, P.-H., Abgrall, R., Breil, J., Loubère, R., Rebourcet, B.: A nominally second-order cell-centered Lagrangian scheme for simulating elastic-plastic flows on two-dimensional unstructured grids. J. Comput. Phys. **235**(C), 626–665 (2013)

[37] Barlow, A.J., Maire, P.-H., Rider, W.J., Rieben, R.N., Shashkov, M.J.: Arbitrary Lagrangian- Eulerian methods for modeling high-speed compressible multimaterial flows. J. Comput. Phys. **322**, 603–665 (2016)

[38] Després, B.: Numerical Methods for Eulerian and Lagrangian Conservation Laws, 1st edn. Frontiers in mathematics. Birkhäuser Cham, Basel, Switzerland (2017)

[39] Maire, P.-H.: A high-order cell-centered Lagrangian scheme for two-dimensional compressible fluid flows on unstructured meshes. Journal of Computational Physics **228**, 2391–2425 (2009)

[40] Toro, E.F., Titarev, V.A.: Derivative Riemann solvers for systems of conservation laws and ADER methods. Journal of Computational Physics **212**(1), 150–165 (2006)

[41] Boscheri, W., Loubère, R., Dumbser, M.: Direct Arbitrary-Lagrangian-Eulerian ADER-MOOD finite volume schemes for multidimensional hyperbolic conservation laws. Journal of Computational Physics **292**, 56–87 (2015)

[42] Boscheri, W., Dumbser, M.: A direct Arbitrary-Lagrangian-Eulerian ADER-WENO finite volume scheme on unstructured tetrahedral meshes for conservative and non-conservative hyperbolic systems in 3D. J. Comput. Phys. **275**, 484–523 (2014)

[43] Boscheri, W., Dumbser, M.: Arbitrary–Lagrangian–Eulerian One–Step WENO Finite Volume Schemes on Unstructured Triangular Meshes. Communications in Computational Physics **14**, 1174–1206 (2013)

[44] Clain, S., Diot, S., Loubère, R.: A high-order finite volume method for systems of conservation laws with multi-dimensional optimal order detection (MOOD). J. Comput. Phys. **230**(10), 4028–4050 (2011)

[45] Barth, T.J., Jespersen, D.C.: The design and application of upwind schemes on unstructured meshes. AIAA Paper 89-0366, 1–12 (1989)

[46] Bauer, A.L., Burton, D.E., Caramana, E.J., Loubère, R., Shashkov, M.J., Whalen, P.P.: The internal consistency, stability, and accuracy of the discrete, compatible formulation of Lagrangian hydrodynamics. J. Comput. Phys. **218**(2), 572–593 (2006)

[47] Balsara, D.: Second-order accurate schemes for magnetohydrodynamics with divergence-free reconstruction. The Astrophysical Journal Supplement Series **151**, 149–184 (2004)

[48] F.Vilar: Cell-centered discontinuous Galerkin discretization for two-dimensional Lagrangian hydrodynamics. Computers and Fluids **64**, 64–73 (2012)

[49] Nikl, J., Kucharik, M., Weber, S.: High-order curvilinear finite element magneto-hydrodynamics I: A conservative Lagrangian scheme. Journal of Computational Physics **464**, 111158 (2022)

[50] Ryu, D., Jones, T.W.: Numerical magnetohydrodynamics in astrophysics: algorithm and tests for one-dimensional flow. Astrophysical Journal **442**, 228–258 (1995)

[51] Torrilhon, M.: Non-uniform convergence of finite volume schemes for Riemann problems of ideal magnetohydrodynamics. Journal of Computational Physics **192**, 73–94 (2003)

[52] Torrilhon, M., Balsara, D.S.: High order WENO schemes: investigations on non-uniform convergence for MHD Riemann problems. Journal of Computational Physics **201**, 586–600 (2004)

[53] Dumbser, M., Balsara, D.S., Tavelli, M., Fambri, F.: A divergence-free

semi-implicit finite volume scheme for ideal, viscous, and resistive magnetohydrodynamics. International Journal for Numerical Methods in Fluids **89**, 16–42 (2019)

[54] Han, J., Tang, H.: An adaptive moving mesh method for two-dimensional ideal magnetohydrodynamics. Journal of Computational Physics **220**, 791–812 (2007)

[55] Fuchs, F., Mishra, S., Risebro, N.H.: Splitting based finite volume schemes for the ideal MHD equations. Journal of Computational Physics **228**, 641–660 (2009)

[56] Orszag, S.A., Tang, C.M.: Small-scale structure of two-dimensional magnetohydrodynamic turbulence. Journal of Fluid Mechanics **90**, 129 (1979)

[57] Jiang, G.S., Wu, C.C.: A high-order WENO finite difference scheme for the equations of ideal magnetohydrodynamics. Journal of Computational Physics **150**, 561–594 (1999)

[58] Gardiner, T.A., Stone, J.M.: An unsplit Godunov method for ideal MHD via constrained transport. Journal of Computational Physics **205**, 509–539 (2005)

[59] Balsara, D.S.: Self-adjusting, positivity preserving high order schemes for hydrodynamics and magnetohydrodynamics. Journal of Computational Physics **231**, 7504–7517 (2011)